Local Liquid Velocity Measurements in Horizontal, Annular Two-Phase Flow

by
Charles R. Kopplin

A dissertation submitted in partial fulfillment of the
requirements for the degree of

Master of Science
in Mechanical Engineering

at the

University of Wisconsin-Madison
2004

Local Liquid Velocity Measurements In Horizontal, Annular Two-phase Flow

Charles R. Kopplin, M.S.
Department of Mechanical Engineering
University of Wisconsin-Madison, 2004
Professor Timothy A. Shedd, Advisor

Two-phase annular flow is commonly used in both commercial and industrial heat transfer; however, we do not yet possess a thorough understanding of the nature of the fluid. Most analytical annular two-phase models are based on a relationship between the liquid film thickness, liquid film mass flux, and the axial pressure gradient or interfacial shear stress. The film thickness calculated from these models can then be utilized to determine the heat transfer coefficient of the flow. Although they are specific to certain flow regimes and fluids, empirical models remain more accurate than these analytical models. The key to understanding these flows lies with the liquid film. Therefore, to better understand the pressure drop and heat transfer of annular two-phase flow, this study involves the development of local, liquid velocity measurement techniques and their application to horizontal, wavy-annular two-phase flow.

Two techniques, Bubble Streak Tracking (BST) and Thin Film Particle Image Velocimetry (TFPIV), have been developed in this study. Utilizing naturally occurring bubbles within the liquid film, the BST technique determines the liquid velocity by measuring reflected light streaks from the bubbles. A three-colored LED array creates directionally unambiguous streaks, while a strobe illuminates interfacial features that affect the liquid velocity. The TFPIV technique applies a typical micro-PIV system to a macroscopic flow with the addition of a non-trivial image processing algorithm. This algorithm successfully overcomes the image noise that occurs when applying PIV to a two-phase, thin film. Although difficulties arise when processing the BST data, the results of the BST and TFPIV methods are comparable, making BST an economical alternative to TFPIV for calculating liquid film velocities.

In this study, these two techniques are applied to horizontal, two-phase flow. These measurements were made in the wavy, wavy-annular, and annular regimes to investigate the mechanism responsible for distributing the liquid film around the tube circumference. The data imply that two of the four major theories are incorrect. While experiments examining the remaining two mechanisms are inconclusive, images from both techniques suggest the waves are responsible for distributing the liquid film.

Lastly, the TFPIV method was used to measure time-averaged velocity profiles within the liquid film of a wavy-annular flow: the first profile measurement of a liquid film at this scale. While the profile at the bottom of the tube is similar to the universal velocity profile utilized in annular two-phase models, the profile at the side and top of the tube exhibit a much different behavior.

Acknowledgements

For the opportunity to conduct these studies and receive this invaluable education, I would like to thank Tim Shedd. Your dedication to my education and research has helped me reach my true engineering potential. I would also like to thank the National Science Foundation for funding my research during the course of my graduate studies.

The people within the Solar Energy Lab have made the last year and a half enjoyable. Of all the friends I have made here, I would especially like to thank my officemates: Adam, Daniel, Diego, Frank, Patty, and Thomas. Thank you for putting up with me; you are all extraordinary people and engineers. I know you will go on to do great things.

I would like to thank Nicolette for her understanding during this process. Without your help and patience, I would not be where I am right now. Thank you for always asking me about my day, even though you know the only thing I will talk about is engineering.

Lastly, I would like to thank my family. My father's interest in my education is beyond that of anyone that I will ever know. My mother's love, concern, and wonderful food have made this experience much easier. Carrie, Lisa, and Brad: Thank you for your interest in both my education and my life in general. I would like to thank Florian, Genevieve, Mary, and Aunt Jane. In your own way, you have kept me on task and reminded me that I am not too far from home.

Sometimes I wonder how I got to where I am today, but it has become obvious that the reasons are the people I have around me.

Table of Contents

List of Figures

List of Table

1 Introduction

Direct expansion evaporators in commercial air conditioning and refrigerating systems, as well as boilers in steam driven power cycles, possess an annular flow of vapor and liquid for much of their length. Currently, it is difficult to accurately model the heat transfer in these applications for multiple reasons; one being that we do not possess a thorough understanding of the liquid velocities within annular, multiphase flows. Throughout the literature, there is no clear agreement upon the mechanisms responsible for the distribution of the liquid film over the circumference of the tube. Although many methods have been used in the attempt to quantify liquid film velocities, very few data exist that describe the velocities in the annular liquid film. Further understanding of the liquid film and the fluid mechanisms within the film will allow the development of more accurate heat transfer models involving two-phase flow for the aforementioned applications.

1.1 Fluid Mechanisms in Horizontal, Two-Phase Flow

Horizontal, annular flow consists of a thin base film flowing along the surface of the tube and disturbance waves that travel over the film at higher velocities. The film is generally smooth with small ripples, while waves are much more turbulent structures.

Although the mechanisms that cause the liquid film to be distributed up the tube walls have yet to be determined, four major theories have been derived from either experiments or flow models.

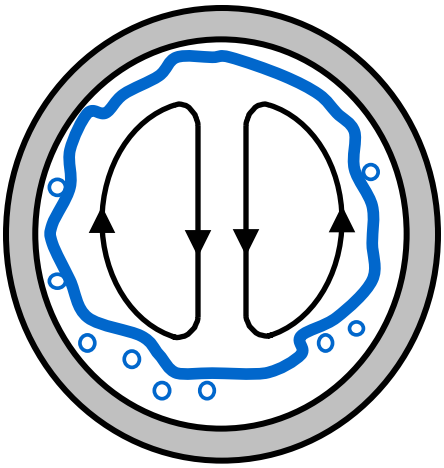

Figure 1.1 Secondary flows in horizontal, annular two-phase flow

During the flow's transition between wavy and annular flow, the liquid film is thickest on the bottom of the tube, thinner on the sides of the tube, and the thinnest on the top. It has also been observed that the disturbance wave height is proportional to the film thickness. The variation in film thickness, along with the disturbance waves, produces an interfacial roughness gradient around the circumference of the tube. This gradient produces a secondary flow normal to the tube axis as was proposed by Pletcher and McManus (1965) and first shown by Darling and McManus (1968). Other experiments have also shown the existence of such flows, including those of Paras et al. (1991),

Dykhno et al. (1994), Jayanti et al. (1990), and Flores et al. (1995). However, the direction and role of these flows in liquid film distribution is still debated.

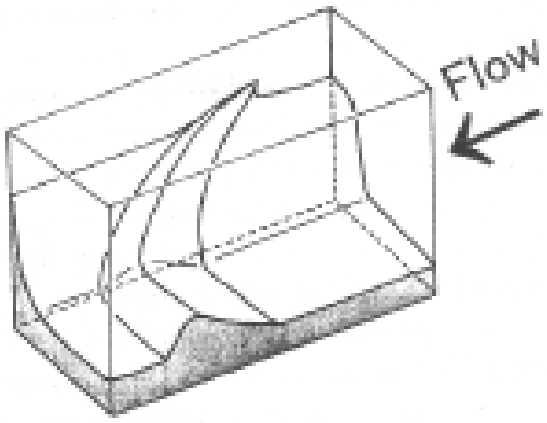

Figure 1.2 Wave spreading mechanism: the film directly in front of the wave is driven up the tube wall (Fukano et al., 1997)

The wave spreading mechanism, which was proposed by Butterworth and Pulling (1972), suggests that as a disturbance wave travels through the tube, it drives the liquid film directly in front of the wave up the tube walls, thus maintaining the film on the top of the tube. The wave spreading theory is based on the idea that the disturbance waves travel faster along the bottom of the tube than along the top. This is thought to create a plowing or wedge effect that pushes liquid film upward immediately in front of the wave.

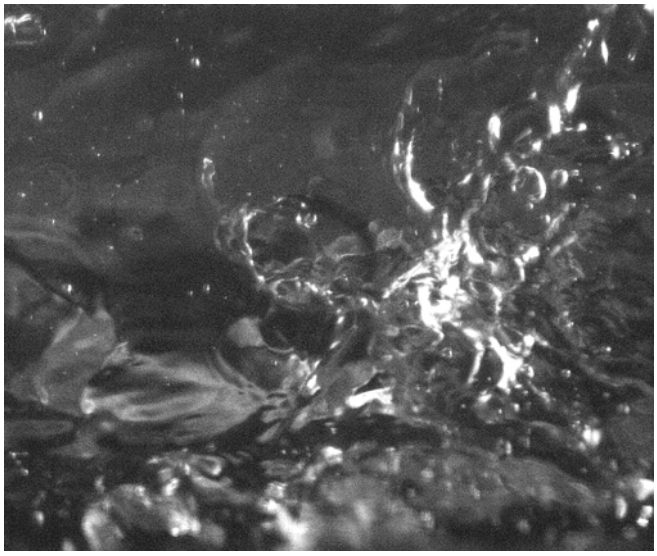

Figure 1.3 Entrainment of droplets from waves in two-phase, annular flow

The formation of the liquid droplets present in the gas core, another liquid transport mechanism, has also been closely examined. It has been shown that the droplets do not form from the entire liquid film, but rather from the disturbance waves [Cousins and Hewitt (1968), Woodmansee and Hanratty (1969), and Azzopardi and Whalley (1980)]. It was first suggested by Russell and Lamb (1965) that these droplets, when deposited onto the top of the tube, could maintain the liquid film around the circumference.

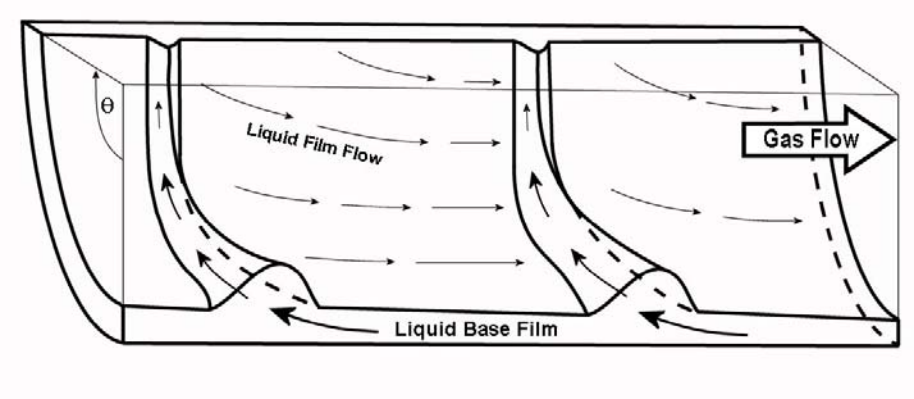

Figure 1.4 Schematic of wave pumping mechanism: liquid within the waves flow up the tube walls, while the film drains downward

Lastly, the wave pumping mechanism was proposed by Fukano and Ousaka (1989). This theory states that the disturbance waves pump the liquid towards the top of the tube through the wave itself. The pumping action results from a pressure gradient along the decreasing height of the wave. Fukano and Inatomi (2003) modeled the transition from stratified to annular flow by direct numerical simulation (DNS). However, it is not clear as to whether the numerical model accurately represents high-quality annular flow where the behavior of the disturbance waves appears to change.

Two of these theories, the two-vortex secondary flow and the wave spreading mechanisms, suggest that the liquid film is distributed around the tube walls due to forces acting on or within the film. The remaining two, the droplet entrainment/deposition and the disturbance wave pumping mechanisms, propose that the liquid is distributed through the center of the tube, i.e., via the air core or disturbance waves.

1.2 Velocity Measurements in Thin Films

Many methods exist for measuring liquid film velocities, several of which are reviewed by Clark (2000). However, when limited to film thicknesses on the order of hundreds of microns, the choice of measurement method becomes very restricted. Because the film is very thin, a non-intrusive measurement method is necessary to prevent any major alterations to the flow. Some choices for evaluation of film velocities in multiphase flow include visualization techniques such as particle image velocimetry (PIV), particle-tracking-velocimetry (PTV), photochromic dye activation (1998), and the more recently developed particle-streak tracking (PST) discussed in Müller et al. (2001).

A number of techniques have been used to gather liquid film velocity data in annular flow. Russell and Lamb (1965) evaluated circumferential and axial velocities by injecting dye and a salt solution into the liquid film and measuring the salt concentration at various circumferential positions. With these average velocities, along with visualization using carbon particles, Russell and Lamb made some observations regarding the distribution of the liquid film. They noted that, on the average, the liquid film travels down the side tube walls with occasional upward motions. These velocities also appeared to be symmetrical about the vertical plane bisecting the tube. Even when the salt solution was injected at the side or bottom of the tube, small amounts of the solution were observed to be present on the top of the tube. Russell and Lamb suggested that this was due to droplets entrained into the gas core and deposited in the liquid film

on the top of the tube. The mechanism responsible for the film distribution was not explored due to their inability to observe the presence of disturbance waves.

More recently, photochromic dye has been utilized by Sutharshan et al. (1995) to quantify liquid film velocities. The dye is mixed with the liquid prior to entering the test section. The displacement over time of a fluorescent spot tracer, created by firing a short pulse of a ultra-violet laser beam through the tube wall, is measured to gather data for both circumferential and axial film velocities. They found that the liquid film travels down the sides of the tube between disturbance waves with the exception of occasional upward movements when a ripple moving that direction passed over the fluorescing spot. They also concluded that disturbance waves play the primary role in the liquid film distribution for the flows examined since the spot moved upward when a disturbance wave passed over it. These experiments have shown important trends in the velocity of the liquid film; however, these observations were not local, and thus can only provide qualitative information about the mechanisms involved in the distribution of the liquid film. Local, quantitative measurements of the liquid film flow are required to develop fundamental models for these complex liquid film flows.

1.3 Overview of Thesis

In this thesis, the development of two velocity measurement techniques is presented. These techniques are utilized to measure average local liquid velocities within

the liquid film in horizontal, annular two-phase flows. The results from these measurements are used to examine the proposed liquid film distribution mechanisms. The velocity profile of the liquid film was also successfully measured with one of the developed techniques. The effect that these profiles have on annular, two-phase modeling is discussed, along with qualitative observations made regarding the waves' role in the liquid film distribution.

2 Bubble Streak Tracking (BST)

Rodríguez and Shedd (2004) have documented the presence of large numbers of small bubbles in the liquid film of wavy-annular and annular two-phase flow. Characterization of these bubbles indicates a relatively constant bubble diameter for a given flow, determined by the wave velocities, that is approximately 20% of the local film thickness. The concentrations of bubbles found by Rodríguez and Shedd are too low to implement PIV from light scattered from the bubbles, but particle tracking and particle streak velocimetry methods may be used. Because of the turbulent and irregular nature of motions in the liquid film, it was felt that a three-color particle streak velocimetry method could be an effective means of extracting local velocities using the naturally entrained bubbles as tracers.

Multiple colors or multiple timing patterns for the light pulses have been used in particle streak velocimetry implementations in the past to provide information about the direction and relative location of particles that cannot be determined from single-color streaks [Sutharshan et al., 1995, Kawaji, 1998, Müller-Steinhagen et al., 2001, Clark, 2002]. The three-color bubble streak velocimetry method used in this study, first introduced by Shedd (2002), is based upon measuring streaks of light reflected by the air bubbles within the liquid film from a three-color LED strobe light. The basic setup is

shown in Figure 2.1. Red, blue, and white LED arrays, assembled in an interspersed manner on a single circuit board, are sequentially pulsed for a predetermined amount of time using a digital pulse generator. The LED arrays and a Xenon strobe light are synchronized with a commercial 3-CCD digital video camera. The Xenon strobe is triggered once per video frame to illuminate both bubbles and interfacial structures within the flow. The result is an exposure that makes it possible to view the bubbles in the liquid and track their velocities for a specified number of cycles (one cycle = Xenon strobe + Red + Blue + White, as an example). Since the method is non-intrusive, it may be easily used at any location along or around a transparent test section.

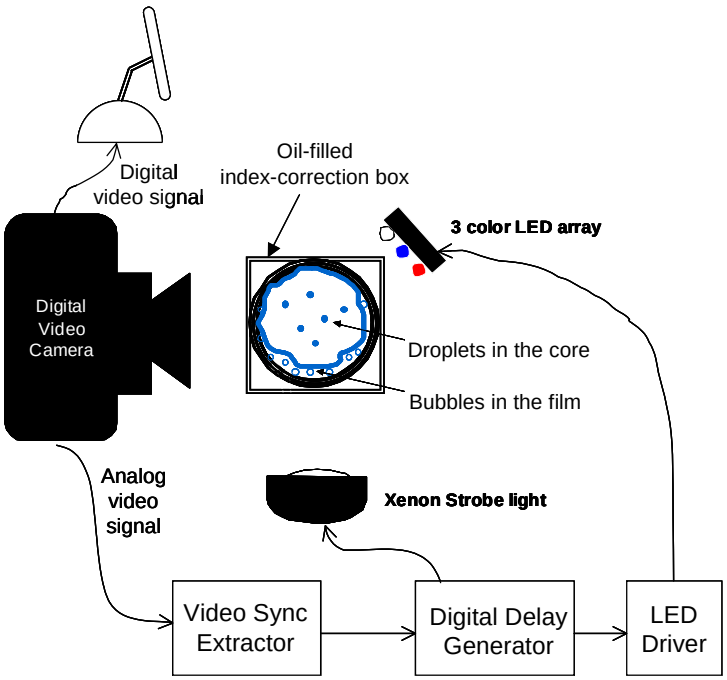

Figure 2.1 Measurement system schematic

As seen in Figure 2.1, a square-sectioned acrylic tube is placed over the PVC test section and the space between the two is filled with vegetable oil. The acrylic and vegetable oil possess indices of refraction similar to that of the clear PVC, and thus minimize the distortion that occurs when capturing images through the curved tube wall. An additional consideration is that the ability to clearly measure the colored streaks is very sensitive to the orientation of the LED arrays relative to the camera. The arrays must be positioned such that they do not produce backlighting or reflections from the air/water interface while illuminating the bubbles enough that reflections are clearly visible to the camera. It has been found that placing the array at approximately 45 degrees from the camera lens axis generally generates acceptable results.

2.1 Bubbles as Tracers

A unique and important aspect of this study is that naturally entrained air bubbles, assumed to represent the liquid velocity, are used as tracers, while methods such as PIV and PTV usually require that particles be seeded into the liquid. Figure 2.2 illustrates typical bubble sizes and length scales in this study. One major concern while using such visualization methods is the particles' ability to accurately represent the flow of the liquid. Although air bubbles are not neutrally buoyant in water, the following analysis suggests that the entrained bubbles are minimally affected by buoyant forces. The buoyant and Stokes drag forces on a bubble can be calculated and used to determine the

resulting circumferential displacement relative to that of a fluid element during the time in which an LED is illuminated. The Stokes solution for drag on a spherical body is

$$F_D = -6\rho\upsilon WR \qquad [2.1]$$

The density and kinematic viscosity of the liquid medium are denoted by ρ and ν, while R is the bubble radius and W is the bubble slip velocity, or the bubble velocity relative to the surrounding fluid.

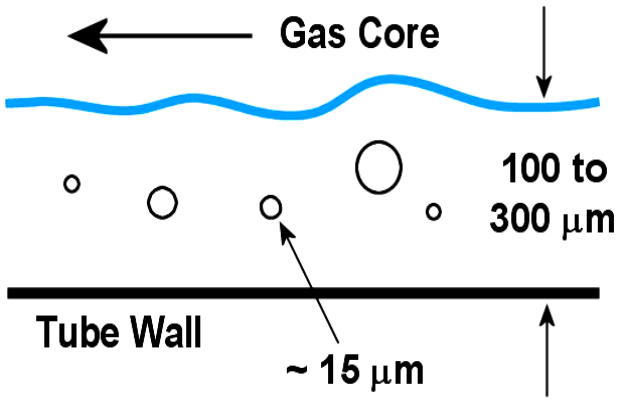

Figure 2.2 Physical scales of bubbles and film thickness in horizontal, annular two-phase flow

For this analysis, the bubble is assumed to travel near the average velocity of the liquid film. Based on the current visualization data and mass balance analyses, the assumption that the Reynolds number based on the slip velocity is quite small appears to be appropriate. The Stokes flow approximation, accurate only for Re < 0.1, can be used as a worst-case estimate since it underestimates the drag coefficient, thus overestimating the drag force if larger Reynolds numbers exist (see Figure 2.3). From this analysis, the

maximum error due to the buoyancy force has been calculated to be less than 0.3 microns for each of the colored streaks, i.e., less than 5% of a pixel width.

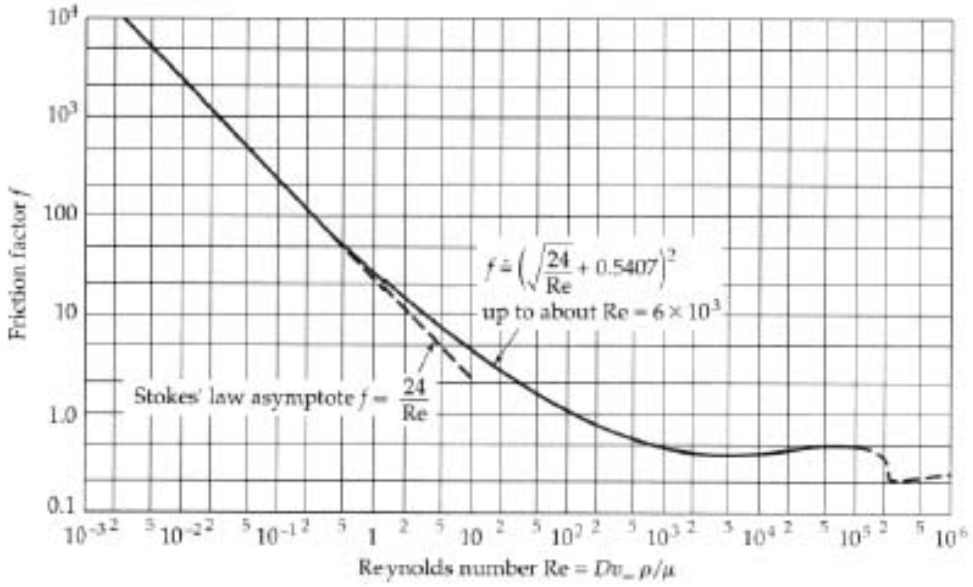

Figure 2.3 Friction factor for flow over a sphere [Bird, Stewart, and Lightfoot, 2002]

2.2 Image Acquisition

A commercial digital video camera with a 90 mm macro lens is used to capture images of the flow at 30 Hz. The three-color LED strobe light implementation uses a Berkeley Nucleonics Model 555-4 digital delay generator with four variable pulse-width outputs. This device generates up to four separate pulses with user-specified pulse-widths, time delays and frequency. A very simple LED driver circuit was used in this work to allow the digital delay generator to drive the relatively high currents required by

each LED array. This driver was composed of a MOSFET transistor and a current limiting resistor (see Shedd, 2002). The width of the light pulse generated by the LEDs driven by this circuit has been measured using a fast photodetector (Thorlabs Inc., Model PDA55) connected to an oscilloscope. Pulse widths as short as 1 μsec could be reliably and repeatably generated with very sharp edges. Thus, the width of the light pulse was assumed to be equal to the width of the pulse generated by the digital delay generator.

The camera shutter speed was set to 0.01667 seconds to allow for a range of pulse-widths to be used without altering the camera setup. However, a continuous exposure for this period frequently resulted in images containing multiple overlapping interfacial features, such as ripples and waves. In addition, the longer the exposure, the greater the number of overlapping streaks, complicating the image analysis. To ensure precise control of the strobe with respect to the camera shutter, the camera and digital delay generator were synchronized. The camera analog video output contains synchronization signals that may be extracted and utilized as trigger pulses. One straightforward way to do this is with a commercially available video sync extraction circuit such as the ZXFV4583 or the LM1881 integrated circuits. With the synchronization signals as inputs to a digital delay generator, it is possible to generate a precise number of pulses per video frame at a precise offset from the beginning of the image.

2.3 Image processing

The video is extracted and separated into 640x480 pixel images using commercial video processing software; these images represent a 4.74 x 3.56 mm area in the liquid film, like the image shown in Figure 2.4. For each flow rate, a minimum of 150 bubble streaks in random images were manually measured using a ruler function in a commercial image processing program. A complication in the analysis arises since the reflections from the bubbles possess a finite width, i.e., a motionless bubble will still produce a streak. However, by measuring the distance from the end of one streak to the end of the next, this zero-velocity streak was eliminated. The images were magnified in the software prior to measurement to minimize the human error to an approximate displacement of two pixels, or 0.015 mm.

The axial displacement, from left to right, as well as the circumferential displacement, from bottom to top, were recorded and converted into bubble velocities for the bottom, side, and top views. A non-zero circumferential velocity for the top and bottom views represents the bubble's movement toward the right (positive) or left (negative) side of the tube, while it would represent a vertical velocity for the side view. Since the liquid film is typically very thin, and the images small, the velocities are considered to be on a Cartesian coordinate system with the horizontal and vertical axes representing the axial and circumferential flow directions, respectively, for all three views.

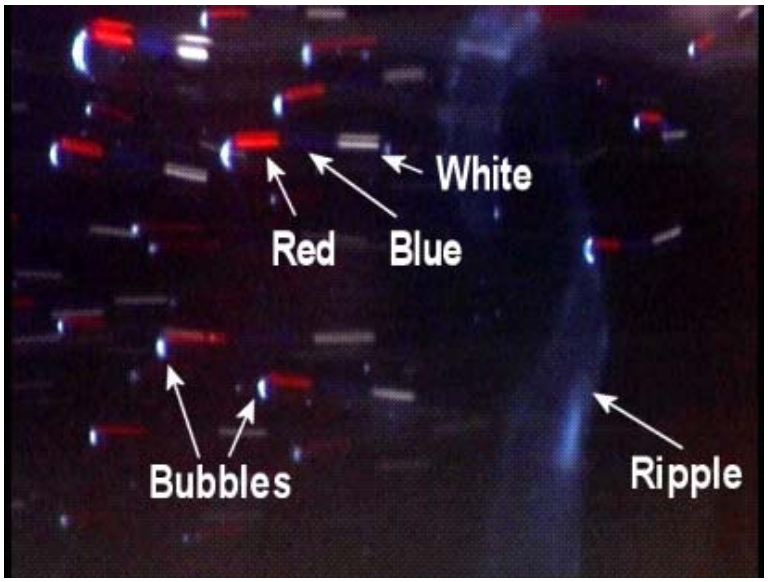

Figure 2.4 Typical video frame (flow from left to right). Light sequence: 1) Xenon strobe, 2) Red LED, 3) Blue LED, 4) White LED

2.4 Air/Water Test Loop

A clear PVC test section, 5.5 m in length and 0.0151 m inside diameter, is used to develop the multiphase flows possessing the qualities considered in the experiment (see Figure 2.5). The measurements are conducted near the end of the section, 330 L/D from the mixing tee, to minimize the effects of combining the air and water flows at the mixing tee. Rotameters are used to measure the air and water volumetric flow rates, while pressure is monitored at the air rotameter outlet to determine a factory supplied flow correction factor. The rotameters possess an accuracy of ±3% of their respective full scales (±0.045 LPM for water, ±7.5 LPM for air up to 250 LPM, and ±42 LPM for air

above 250 LPM). Flows have been tested for air flow rates from 100 to 400 LPM and 0.5 to 1.5 LPM for water. This has produced data for a range of flow qualities from 0.07 to 0.49.

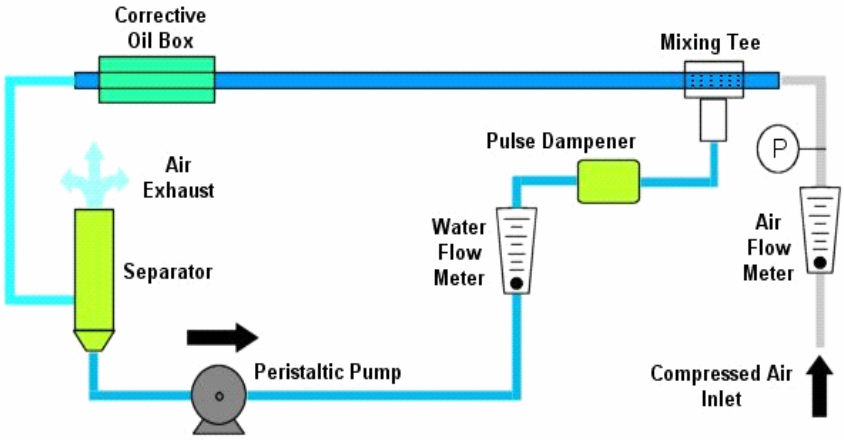

Figure 2.5 Diagram of Air/Water Loop

2.5 BST Results

The data obtained in this experiment can be evaluated by examining the average measured velocities of the bubbles. Since the flow is assumed to have reached steady state by the time it is evaluated (330 L/D from the liquid entrance), a mass balance should exist between the liquid flowing up the sides of the tube and the liquid flowing downward if strong secondary flow or wave spreading mechanisms exist. Therefore, the average measured circumferential velocity of the bubbles within the film should equal zero at a

given circumferential position. If this is not the case, then the data suggest the liquid is not distributed to the top of the tube via the liquid film.

The average axial velocities are plotted against flow quality, *x*, (the ratio of air mass flow rate to total mass flow rate) in Figure 2.6a. The maximum and minimum estimated variation for the data set (with 95% confidence) for the three views is also shown. This variation includes the error incurred through the manual measurements (± 2 pixels), but generally represents the variation in the measured bubble velocities. Although an obvious trend does not exist, it is useful to note the relationship between the top, side, and bottom average axial velocities. The average axial velocity is always largest at the bottom of the tube, and the average axial velocity at the top is the smallest in all but one of the flow qualities. Except for the very low qualities, the difference between the average axial velocities at the different views decreases with increased flow quality. As the flow quality increases, the flow moves further into the annular regime where the difference in liquid film thickness at the top, side, and bottom of the tube also decreases (see Hetsroni, 1982). The data suggest that as the liquid film becomes more evenly distributed, the average axial velocity gradient around the circumference of the tube decreases.

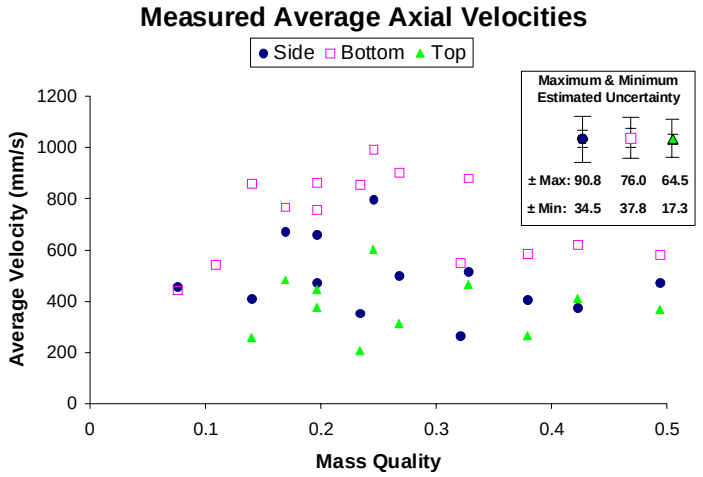

(a)

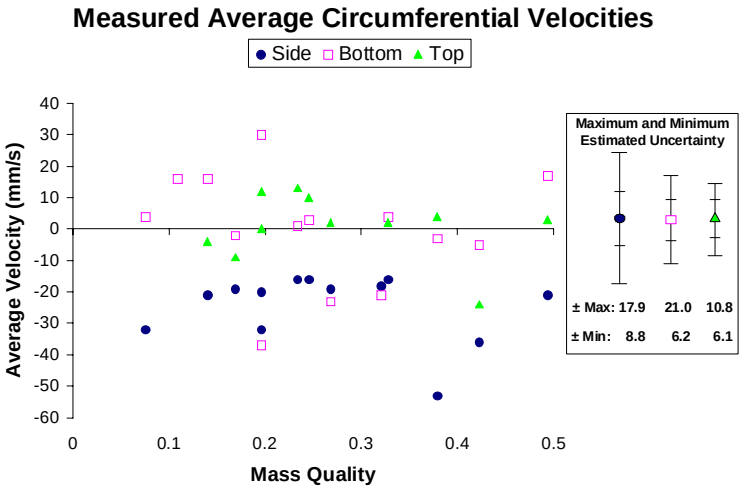

(b)

Figure 2.6 Measured average a) axial and b) circumferential velocity vs. mass quality with maximum and minimum variation (estimated with 95% confidence)

Figure 2.6b shows the average circumferential velocities plotted against flow quality along with the maximum and minimum uncertainties for each data set. No trends exist for the top and bottom views: the average velocities travel to either side of the tube in no particular pattern. All of the average circumferential velocities at the side view are downward, suggesting draining to the bottom of the tube; however, upward flow does lie within the maximum uncertainty range, indicating that there can be significant instantaneous upflow in the film. One should note that the uncertainty bars show that the variation in measured circumferential velocities at the side is much larger than at the top and bottom. This is due to the variation in circumferential film velocity induced by ripples and disturbance waves.

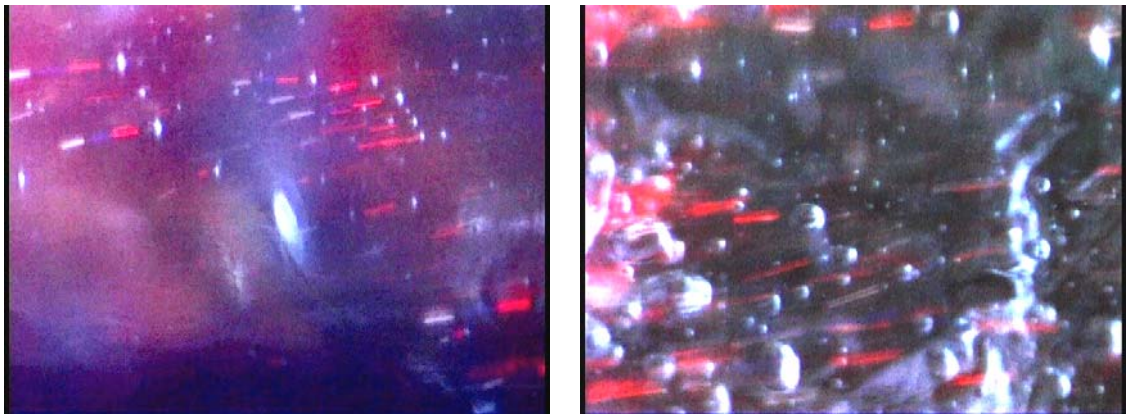

a) *b)*

Figure 2.7 Interfacial features within BST images: a) ripple in the center of the image, b) the back end of a wave (flow is from right to left)

The Xenon strobe is flashed once per video frame, illuminating both the entrained bubbles and interfacial features (see Figure 2.7). Such features include ripples and

disturbance waves. This allows each video frame to be characterized by interfacial features into one of three categories: smooth, ripple, or wave. By designating the frames in this manner, the effect of these features on the liquid film velocity can be monitored.

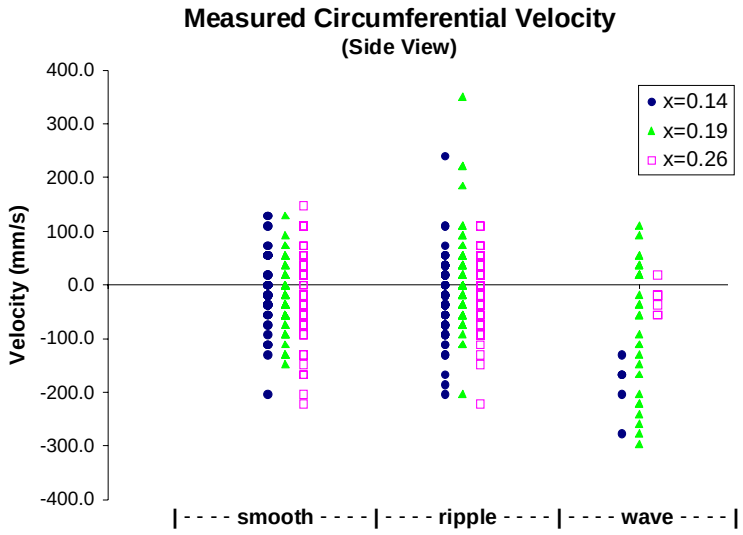

Figure 2.8 Side circumferential velocity data for various flow qualities

Figure 2.8 presents data plotted in the aforementioned manner for multiple flow qualities. These data show that the circumferential velocity at the sides of the tube is not dependant upon flow quality, as is the case with the data on the whole. The largest circumferential velocities occur in the ripple and wave images showing the significant effect these features have on the liquid film. However, these large velocities are both positive and negative throughout the acquired data, causing the average circumferential velocity to be close to zero for frames possessing these features. This implies that these flow features do not distribute the liquid film by forcing it up the sides of the tube wall.

Another interesting point can be made by solving the Navier-Stokes equations for laminar flow, neglecting interfacial shear forces, for a gravitationally driven, thin liquid film flow down a flat plate. To simulate the flow down the sides of the tube where the images are collected, the plate is assumed to be vertical. Using film thickness measurements obtained for these flow conditions (see Shedd, 1998), one can calculate the average film velocity, $\overline{V}$, using Equation [2.2].

$$\overline{V} = \frac{\rho g \sin\theta}{\mu} \frac{h^3}{3} \qquad [2.2]$$

The density and dynamic viscosity of the liquid are denoted by ρ and μ respectively, θ represents the angle of the plate, and h is the film thickness. A plot of the measured side circumferential data compared with calculated average film velocities for the corresponding flow rates can be found in Figure 2.8. The draining velocity generally decreases with increasing quality due to thinner liquid films at higher qualities. For the lower qualities examined in this experiment, this model predicts downward circumferential velocities that are nearly two times the experimental data. However, for the qualities above 0.4, the calculated draining velocity falls within the uncertainty range of the experimental data.

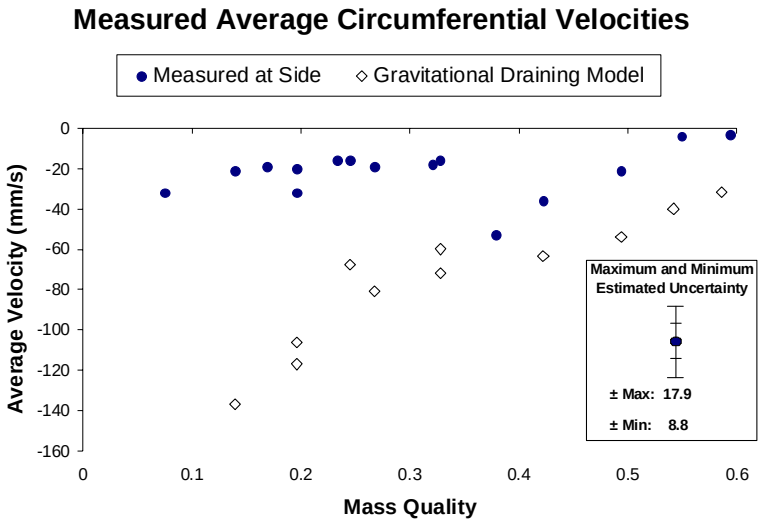

Figure 2.9 The measured side circumferential velocities and calculated gravitational draining at corresponding flow rates

2.6 Discussion of Fluid Mechanisms

As previously discussed, two of the proposed liquid film distribution mechanisms act through the base liquid film, while the other two suggest the liquid is distributed through the gas core (as droplets or in waves). These average velocity measurements allow the evaluation of two of the proposed mechanisms, while the remaining two mechanisms are discussed.

2.6.1 Secondary Gas Flows

Secondary gas flows are generated by turbulence and are typically on the order of 4% of the axial flow in magnitude (Flores et al., 1995). Thus, though there appears to be

some factor countering gravity at the lower qualities, it does not seem physically reasonable to attribute such a significant difference to secondary flow effects. Based on the current observations, it is more likely that the upward flow countering gravity is due to upward-flowing ripples. The low quality flows examined in this experiment ($x < 0.5$) appear to possess a smooth air-water interface at the side of the tube. This smooth surface periodically possesses ripples that cause sudden changes in circumferential bubble velocities as they pass over the bubbles. The air-water interface for the higher quality flows ($x > 0.5$) appears to behave differently; nearly all images include an interfacial structure. These structures appear similar to the ripples in lower quality flows, but they produce a smaller circumferential bubble velocity gradient, perhaps because the ripples, though more frequent, are smaller and have more random orientations.

2.6.2 Wave Spreading

It is very difficult to decipher any bubble streaks in the images that include disturbance waves. The large bubbles and complex air/water interface cause large stray reflections, overwhelming most bubble streaks in the image. If a bubble within a disturbance wave appears to be in focus in an image, its streak will often be difficult or impossible to measure accurately. The wave images in which streak measurements are made usually possess only the front or end of the wave. This is precisely the region where the wave spreading theory suggests strong upward flow of the film driven by the oncoming wave. Since the average circumferential velocities outside of the waves are

nonzero and predominantly negative, the existing data suggest that wave spreading is not a plausible explanation for the liquid film distribution.

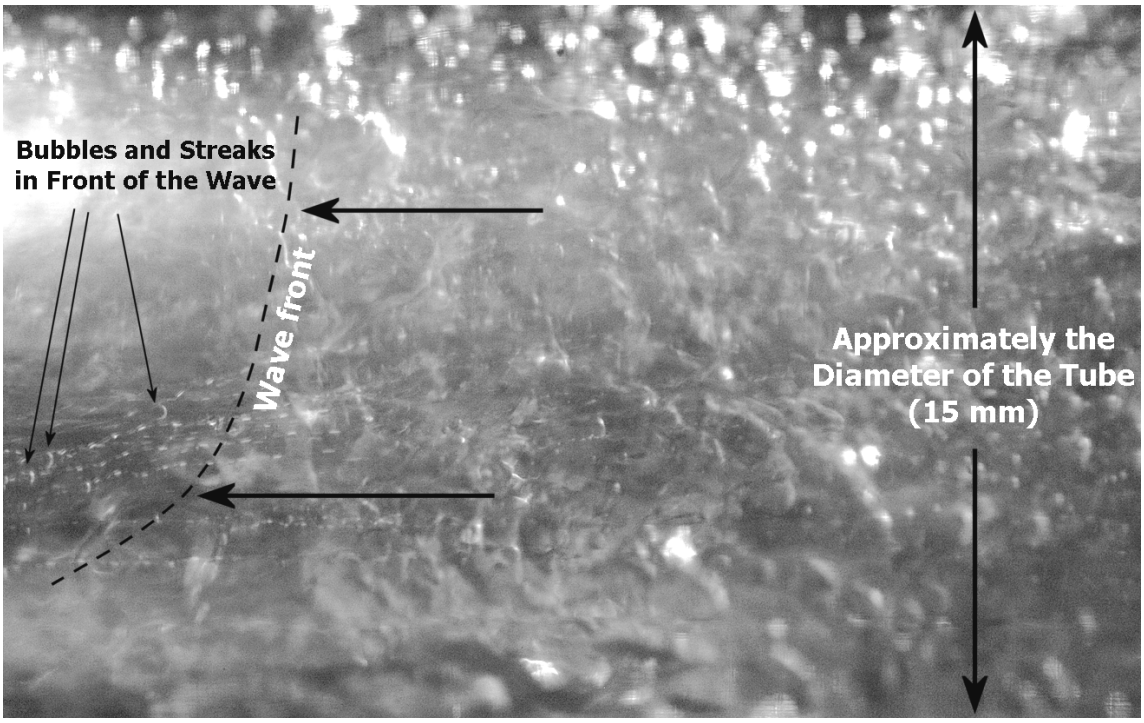

Figure 2.10 Bubble streaks moving down the tube walls directly in front of a wave (flow is from right to left)

Qualitative BST images can also be taken at a larger scale such as the image in Figure 2.10 taken through the side of the tube. In this image, the Xenon strobe has illuminated a disturbance wave as well as a few bubbles in the liquid film directly in front of the wave. The bubble streaks created by the LEDs show that the bubbles possess a downward motion immediately in front of the wave, implying that the wave spreading mechanism is not present in this flow.

2.6.3 Entrainment/Deposition

It is well known that liquid droplets exist within the air core in horizontal, annular flow. It has also been shown that these droplets are formed predominantly at the surfaces of the disturbance waves (Azzopardi, 1997). Droplets are entrained in the air core and eventually deposited in the film. Some believe this mechanism to be the primary source of the liquid distribution. A simple model, based on a correlation of the results of several experiments, has been produced by Stevanovic and Studovic (1995). This model was derived from vertical annular flow data; however, it was utilized in this study, as it has by others, to estimate the liquid droplet deposition rates for horizontal annular flow. This model has been used to estimate the net entrainment in the air core and droplet deposition on the top half of the tube for the flow rates tested in this experiment. The mass flux due to deposition was then compared to the mass flux down the tube wall calculated with the average side circumferential velocity and film thickness.

The downward mass flux in the liquid film calculated from the measured data is over 40 times the droplet deposition mass flux calculated with the droplet model for the lower quality flows ($x < 0.5$), but only eight times larger for the high quality flows ($x > 0.5$). This suggests that the entrainment/deposition mechanism may become a more significant means of liquid distribution as the flow moves further into the annular regime. However, differences of this magnitude still suggest that entrainment/deposition is not the primary liquid distribution mechanism.

2.6.4 Wave pumping mechanism

This mechanism proposes that the liquid within the disturbance waves travels upward due to a circumferential pressure gradient, thus distributing liquid to the top of the tube. It also suggests that the liquid film drains toward the bottom of the tube due to gravity after the passage of each wave. Since the bubble velocities within the disturbance waves and liquid film could not be measured simultaneously, this experiment is unable to provide clear evidence that this is the dominant liquid distribution mechanism. However, having essentially eliminated the preceding three mechanisms, it appears that this mechanism warrants further detailed study.

2.7 Summary

A novel, inexpensive velocimetry method for use in thin liquid films has been presented in this chapter and applied to liquid films occurring in a wide range of air/water annular flow conditions. For the first time to the author's knowledge, local liquid velocity measurements have been obtained for annular flow at the top, side and bottom of a horizontal pipe. In light of these measurements, four of the commonly cited theories for liquid distribution in annular flow have been evaluated. For the experimental conditions studied, wave spreading and secondary gas flows are unlikely to contribute to the flow of liquid upwards at the wall. Droplet entrainment and re-deposition appears to

contribute at high-quality conditions, but still seems to be a minor effect. This leaves flow within waves as the primary vehicle for the upward liquid motion.

This experimental method, however, leaves significant uncertainty as to the actual velocity in the liquid film. While the bubbles were shown to be adequate tracers, they are large with respect to the liquid film thickness and therefore present some average velocity corresponding to their location in the film. Cross-sectional images of the liquid flow indicate that the bubbles may be somewhat randomly distributed throughout the upper 2/3 of the film (Rodríguez and Shedd, 2004), suggesting that the observed velocities represent a random sampling throughout the upper part of liquid layer. While sufficient samples were obtained to allow for some confidence that the measurements represent an average of the film velocity, the bubble streak measurements will be biased toward the higher velocities that occur nearer the air/water interface and significant uncertainties remain.

Given these issues, a more accurate and even more local measurement is desired. To address this, micro-scale Particle Image Velocitmetry techniques were adapted to the flow geometries occurring in annular flow, as described in the next chapter.

3 Thin Film Particle Image Velocimetry (TFPIV)

Many of the equations used to predict the pressure drop and heat transfer in two-phase annular flows are heavily correlated. As a result, these equations are usually accurate only for specific flow parameters and flow regimes. However, these correlations are the most accurate models that exist since the mechanisms within such flows are not well understood. Common phenomenological pressure drop and heat transfer models for two-phase annular flow assume a turbulent boundary layer profile, but it has yet to be determined whether the film should be modeled as laminar, unsteady viscous, or turbulent. Similar to a turbulent boundary layer, the film possesses a relatively large velocity gradient across its thickness. However, unlike a turbulent boundary layer, the gas-liquid interface dampens turbulent momentum transfer while the turbulent gaseous core contributes fluctuating velocities through the generation of waves and ripples.

In order to better understand the nature of the liquid film in horizontal, annular two-phase flow, the objective of this study is to obtain the average liquid film velocities about the circumference of the tube and examine the velocity profiles of the film. Observation of these velocities provides a sense of the turbulent nature of the film and more refined examination of the liquid distribution mechanisms. Through the

development and utilization of thin film particle image velocimetry (TFPIV), first introduced by Shedd (2001), this experiment is the first successful study of annular two-phase flows using PIV in the literature and the most highly resolved velocity measurements in the liquid film of annular two-phase flow.

3.1 PIV Background

Particle image velocimetry (PIV) is a well-established method for measuring fluid velocity fields [see, for example, Adrian, 1991 and Raffel et al., 1998]. A typical PIV experiment consists of a fluid flow seeded with tracer particles. A camera is utilized to capture two exposures of these particles within the flow separated by a specified, short delay. The double-exposed images, or pairs of single-exposed images, are divided into interrogation regions, and the displacements of these regions are statistically estimated by correlating the pairs of particle images. These particles appear as intensity peaks or voids depending on the experiment. The particles can be detected as voids if the flow is backlit. Traditionally, however, particles are detected by the light they scatter as they pass through a planar light sheet in the flow. In addition, particles can be purchased that fluoresce when exposed to certain wavelengths of light, emitting a different wavelength light.

The advancement of digital technology has led to the application of PIV to new types of flows. Micro-PIV was first introduced by Santiago et al. (1998) in the study of a

Hele-Shaw flow over a microscopic elliptical cylinder. Prior to this group's experiment, researchers had been utilizing macroscopic camera lenses to analyze macroscopic flows. Since then, micro-PIV has been expanded to other microfluidic systems, such as flow through micro-channels [Meinhart et al., 1999] and micro-electromechanical systems (MEMS) [Meinhart et al., 2000].

Because of its ability to acquire instantaneous velocity fields, instead of data at discrete points, particle image velocimetry has been adapted to other complex flows, such as two-phase flows, whose mechanisms are not yet fully understood. This has led to the development of many methods that simultaneously conduct PIV on multiple phases. Many novel techniques have been created to differentiate phases within a PIV image. These techniques range from very simple methods, such as differentiation by color [Towers et al., 1999], to more complex methods such as applying an image mask in which second order derivatives of the intensity are calculated [Khalitov & Longmire, 2002].

The aforementioned techniques have been applied throughout the literature to a wide range of two-phase flows. PIV has been applied to liquid/gas flows in fuel sprays [Driscoll et al., 2003], solid/liquid flows during sedimentation [Kiger and Pan, 2000], and, as in the current experiment, gas/liquid flows, such as vertical bubbly pipe flows [Hassan et al., 1998, Choi et al., 2001, and Lindken, 2002]. These bubbly flow studies have successfully compared bubble velocities and the velocity of the surrounding liquid through the marriage of novel measurement techniques and PIV.

3.2 Particles in Two-Phase Annular Flow

Ideally, the seed particles should possess a similar density to that of the fluid and possess a minimal diameter. This is done to ensure that a particle accurately represents the velocity of the surrounding fluid element and therefore maximizes the PIV experiment's accuracy. Particles possessing densities within a few percent of typical liquid media are now commercially available; however, the particle diameters used throughout the literature are specific to the experiments. The limit to the minimum particle size for a typical experiment is a function of image magnification, resolution, allowable measurement error, or a combination of the three. There has been a considerable amount of work within the literature to determine the relations that optimize these PIV parameters.

By testing images from Monte Carlo simulations, Westerweel (1997) has shown that the measurement resolution is not determined by the size of a pixel, but by the particle-image diameter relative to the size of the interrogation region. There exists an optimal particle image diameter, after which increasing the resolution will only result in over sampling of the data. This optimal particle image diameter was determined to be two pixels by Prasad et al. (1992).

As the size of the particles used in PIV experiments approached the order of the wavelength of the light used to illuminate them, a relation for the diffraction limited particle image diameter was determined [Adrian, 1991]. Relations for image spot size (Equation [3.2]) were developed, which is the convolution of the Gaussian geometric particle image and the diffraction limited spot size. The diffraction limited spot size relation, based on the first dark ring of the Airy function, was further developed by Meinhart et al. (2003) for PIV systems utilizing infinity corrected microscope objectives. The equations for diffraction spot size, $d_{s,\infty}$, and diffraction limited spot size, d_e, are given by

$$d_{s,\infty} = 1.22M\lambda\sqrt{\left(\frac{n_o}{NA}\right)^2 - 1} \qquad [3.1]$$

$$d_e = \sqrt{M^2 d_p^{\,2} + d_{s,\infty}^{\,2}} \qquad [3.2]$$

In these equations, M=10 is the magnification, λ=612 nm is the wavelength of the fluoresced light, n_o=1 is the index of refraction of the immersion medium, NA=0.28 is the numerical aperture of the microscope objective, and d_p=500 nm is the geometric particle diameter. The particle diameter for this experiment is calculated to be 2.6 pixels. However, these equations assume a Gaussian profile for the image. Non-zero background intensities will eliminate the edges of this profile, causing the particles to appear smaller than the calculated value. Since interfacial flow features cause strong fluctuations in background intensity, the particle image diameter has been noted to vary

by ±1 pixel in the actual images of this study. The particle images also vary depending upon whether or not the particles are in-focus. The particle image diameters of out-of-focus particles will be discussed in Section 3.6 where the depth of field is defined.

3.2.1 Effect of Particles on the Flow

Considering the effect of these particles on the flow itself is also vital to the TFPIV experiment. If too many particles are present, the characteristics of the flow itself could change, thus defeating the purpose of the experiment. The magnitude of the particles' effect not only depends on the particle concentration, but also on the velocity gradients in the fluid. For instance, in this experiment, a thin film under high shear is being examined. The average velocities and velocity profiles measured in this experiment are very dependant upon the shear within the film, i.e., effective fluid viscosity. If the particles create an effective viscosity much different than the actual fluid viscosity, the velocity profile and turbulence of the film will be affected. The dampening of fluid turbulence by particles has been documented within the literature [Yarin and Hestroni, 1994, Crowe et al., 1996, Chen and Pereira, 1999, Ooms and Jansen, 2000].

To determine the effect of the particles on the nature of the two-phase annular flows examined in this study, measurements of pressure drop were conducted over the range of liquid and gas phase flows studied in the PIV measurements. The same test section was used for these measurements, which were conducted both with and without particles in the liquid.

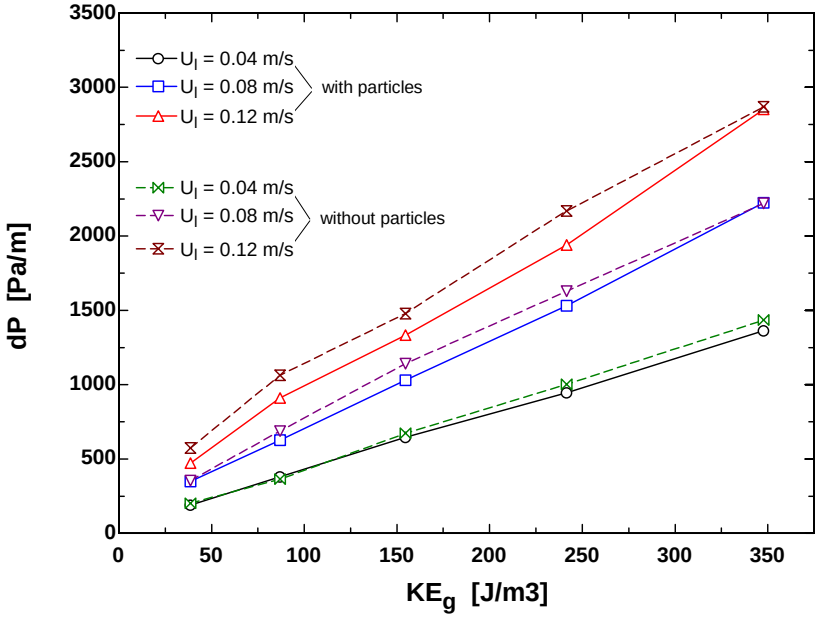

Figure 3.1 Measured test section pressure drop vs. the kinetic energy of the gas with and without seed particles

As shown in Figure 3.1, the measured pressure drop is consistently higher for the test cases without seed particles. The percent difference between the two flows remains within 6%, 10%, and 17% for U_l equal to 0.04, 0.08, and 0.12 m/s, respectively. These numbers are somewhat larger than the uncertainty in the differential pressure measurements (approximately 5% of reading), so the differences provide some reason for further analysis.

3.2.2 Particle Distribution within the Film Thickness

Minimization of particle size not only maximizes the measurement system's accuracy, but it also allows for the most uniform particle distribution throughout the film thickness, which is optimal for this PIV experiment. It has been shown by Kraftori et al.

(1995) that the particle position in a turbulent boundary layer is a function of both particle density and particle diameter. It was shown that, in general, the velocity of the particles increasingly lagged that of the fluid as particle diameter increased. Kraftori et al. also noted that the particles tended to settle in areas of slow fluid velocity, namely near the wall. Mei and Hu (1999) noted that particles also tend to move towards fluid with low vorticity, which should drive particles away from the wall in these experiments. Although the liquid film is often modeled as a turbulent boundary layer, one might expect a different particle distribution since the liquid film in two-phase annular flow never reaches a fully developed state. It is constantly affected by the gas core, disturbance waves, and deposited droplets. These mechanisms most likely enhance mixing of the particles within the liquid and prevent any settling of particles towards the wall.

PIV images were acquired throughout the thickness of the liquid film for a typical wavy-annular flow and it was verified that the particles remain uniformly distributed within the film. The experimental setup is described in detail below, but briefly, the camera was mounted on a digital micrometer translation stage. The camera was originally focused on particles on the tube wall at the side of the tube and was then translated in toward the tube wall. Images were taken throughout the thickness of the film for a flow of 300 LPM of air, and 0.2 LPM of water. Near the wall, the camera was stepped at five micron increments until the image plane was located approximately twenty five microns from the wall. The increment step size was then increased to ten microns for distances beyond twenty-five microns from the wall.

While focused on the tube wall, a few moving particles appeared along the center of the image, and as the camera was focused from five to fifteen microns from the wall a full field of dispersed particles appeared in the PIV images. Beyond fifteen microns from the wall, particles were noted throughout the images until the plane of focus moved within range of passing ripples on the gas-liquid interface. At this point, recessed regions (troughs of ripples) could be identified by large out-of-focus particles without the presence of intense, in-focus particles. The effect of ripples was observed between roughly 150 to 200 microns from the tube wall, which corresponds to an approximate film thickness at the side wall for this flow. PIV images were taken beyond these distances from the wall, which occasionally captured the motion of particles within the waves, demonstrating that TFPIV can be used to determine wave velocities and turbulence within waves.

The location of the maximum particle density was found to vary depending upon the liquid film thickness and flow rate. In general, a higher particle density was achieved for higher liquid flow rates. The data collected for the average liquid film velocities was taken at a distance between 70 and 80 microns from the wall. Within this range, the depth of field remained within the liquid film at all times for all of the flows tested.

3.3 Experimental Setup

The experimental setup for the PIV measurement system is nearly identical to that of bubble tracking velocimetry (BTV) experiment described in Chapter 2; however, the test section is made of quartz tubing possessing a 23 mm inner diameter. The flow travels 5.8 m, about 250 L/d, inside the test section prior to being measured by the TFPIV system. A square-sectioned quartz tube was once again placed over the round tube and the gaps between the two filled with oil possessing a similar index of refraction. The oil box minimizes any distortion by taking images through the curved walls of the tube. This experiment used polystyrene particles impregnated with fluorescing dye possessing a diameter of 500 nm and purchased from Duke Scientific, Inc. A rotameter was utilized to control the air volumetric flow rate into the test section, and the water flow rate is controlled by a peristaltic pump and measured via a turbine flow meter.

The visualization setup can be seen in Figure 3.2. The camera is mounted on a two-axis micrometer stage connected to a rigid aluminum frame. The test section is also clamped to the aluminum structure to minimize the effect of flow-induced vibrations on the PIV measurements. This setup can be rotated about the tube axis such that images can be collected through the side, top, and bottom of the tube. Unlike typical PIV methods, TFPIV does not utilize a thin laser sheet to illuminate the particles within the depth of field. The curved quartz tube walls create a complex optical path for a thin sheet, and the liquid film itself is thinner than a typical PIV laser sheet. Instead, the plane

illuminated by the laser is limited by the thickness of the film when the flow is flooded with the laser light through a beam expander. It was also found during this experiment that particles were the most defined when illuminated from the same side of the tube as the camera. This caused the particles to fluoresce the brightest, suggesting that a confocal setup would be ideal for future experiments.

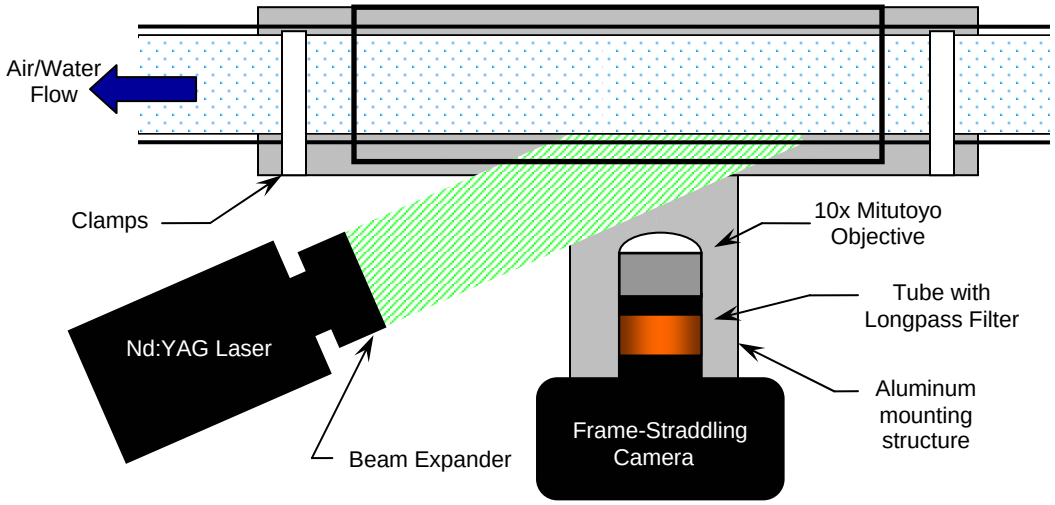

Figure 3.2 TFPIV measurement system setup

The laser used in this experiment is a New Wave Research Solo PIV Nd:YAG laser. A Roper Scientific 1300YHS-DIF camera with a 1300 x 1030 pixel CCD sensor collects the images through an infinity-corrected 10x Mitutoyo microscope objective (NA = 0.28) and a longpass filter that blocks the green laser light (see Figure 3.2). A Princeton Instruments 5MHz MicroMax Controller interfaces the camera with the controlling computer. The images taken with this system are 1.625 mm x 1.29 mm possessing 1.25 μm/pixel resolution.

Once the particles are exposed to the 532 nm (green) light from the laser, they emit red light with an emission maxima at 612 nm, as specified by the supplier. The amount of time in which the particles continue to fluoresce after the laser pulse is on the order of nanoseconds, so motion-induced blurring of the particles does not occur in the PIV images. The filter between the objective and camera allows the fluorescent red light to pass, while preventing the green laser light from passing through to the CCD.
The laser and camera are synchronized by signals from a digital pulse generator (Berkeley Nucleonics Corp. Model 555-8). The camera is operated in Internal Exposure Control mode such that only one input signal is required to trigger the collection of the two TFPIV images. The first image is acquired and stored, and the second is taken immediately after. Only after the second image is acquired are the two images sent to the computer software. Two pulses trigger the flash lamps of each laser, which stimulate the Nd:YAG crystal. Another two signals are sent 185 μsec after the flash lamp signals to trigger the Q-switch of the first and second lasers. The cycle is repeated once the camera controller sends a signal to the pulse generator that the images have been sent to the software. Typical widths and delays of these signals are listed in Table 1.

Digital Pulse Generator Settings*			
Channel	Trigger for:	Width (μsec)	Delay (μsec)
1	camera	100	170
2	1st flash lamp	100	0
3	2nd flash lamp	100	50
4	1st Q-switch	100	185
5	2nd Q-switch	100	235

*for an exposure time of 50 μsec

Table 1 Typical digital pulse generator settings used in TFPIV experiment

The signals to both the camera and laser are triggered via the rising edge. The camera exposure was varied between 50 and 100 μsec, but the delay between the two lasers sets the time difference between the single exposure PIV images. While this delay was varied between 20 and 90 μsec to account for varying liquid film velocity, the camera exposure was only varied to assure that the laser fired near the middle of the exposure. One should also note that both signals are sent to the lasers before the signal to the camera. This laser model requires between 180 and 210 μsec after the Q-switch for the laser to fire. By varying this signal delay, the delay was determined to be approximately 180 μsec for this specific laser.

3.4 Image Pre-Processing

TFPIV images can possess features of the film that can influence the velocity vectors. Bubbles within the film can be seen in the images. Since the particles are

excited by flooding the test section with the laser as opposed to the use of a laser sheet, the particles act as an ambient light source throughout the film. Some of this ambient light will be reflected by bubble interfaces into the microscope objective. This causes the outline of the entrained bubbles to appear in the images. Particles coalescing at the interface of larger bubbles have also been observed in these images. If these coalescent particles or the outline of any bubble exists in an image, the resulting PIV vectors in the coinciding interrogation areas will represent the velocities of the bubbles rather than the liquid film. The bubble slip velocities within such liquid films have not yet been precisely determined, and therefore the coalesced particles and bubble outlines should be excluded from the PIV vector calculations.

Ripples on the film interface and waves passing over the film affect the contrast of the TFPIV images. The ripples produce intensity gradients within the image. This effect is most likely due to a ripple's tendency to possess more particles than the rest of the film, and the sloped interface of the ripple reflecting fluorescent light into the camera. The areas of the image possessing ripples generally have higher average intensities than those without. Images in which waves are passing over the film have a higher average intensity than those with ripples or no flow features. Sharp intensity gradients, similar to those produced by ripples, exist within these images as well. These gradients are a result of complex gas-liquid interfaces within the waves. With these variations of intensity within the images, it is possible that some of the particles will not be visible to the PIV software during vector calculation. Some particles may be too dim relative to the rest of

the image, while others may be too dim relative to a local intensity peak occurring in the proximity of an interfacial feature.

The presence of bubbles, ripples, and waves within the images can produce erroneous vectors and the exclusion of particles within the film. In order to evaluate the local liquid velocities within the film, the bubbles and sharp gradients in image intensity must be eliminated. These effects, along with unavoidable dark noise resulting from the use of a digital camera, require that the TFPIV images be processed prior to the vector calculation.

3.5 Image Processing Techniques

Throughout the literature, many phase discrimination techniques are utilized for simultaneous PIV measurements. Towers et al. (1999) used particles that fluoresced at different wavelengths, while Sakakibara (1996) utilized an intensity threshold and particles whose fluorescent intensity was a known fraction of that of the other dispersed, solid phase. Many research groups have used a technique similar to that of Lindken and Merzkirch (1999), who utilized spot size to differentiate from the tracer particles and the dispersed gas phase. Later, Kiger and Pan (2000) discriminated via spot shape; bubble reflections, which appear as rings rather than solid circles, can be discriminated from particles that possess only one intensity peak. Utilizing the fact that one phase was moving much faster than the other, Rottenkolber et al. (1999) separated air and water

droplets by the height and width of the correlation peaks. Lastly, Khalitov & Longmire (2002) applied a mask to the images that calculated the second order spatial derivative of the natural log of intensity. They found that this method allowed for separation of both different sized particles and as well as those of different intensity. Image processing methods have also been developed to overcome background noise and background intensity gradients [Tian and Qiu, 2002]. However, due to the presence of bubbles and background intensity gradients, further processing is required for images in the present study than is described within the literature. Several steps are taken during the processing of TFPIV images to eliminate the aforementioned film features from the images. The image processing techniques described in this section have been implemented into a single macro for use with the LaVision DaVis software. However, knowledge of these techniques will be useful for other TFPIV applications [see Russ, 1999].

3.5.1 Image Processing Functions

Median Filter – The artificial objects smaller than the particle images are removed first. Dark noise must be eliminated since it typically produces objects one or two pixels in size. This noise could be mistaken as a particle and thus lead to incorrect vector calculations. Since the particle size in this experiment was chosen such that they appeared to be three or four pixels, a median filter is utilized to eliminate all objects two

pixels in size or smaller from the image. Applying this filter early in the post-processing has been found to produce the best results.

Gaussian Smoothing – A copy of this image is made within the software, and a Gaussian kernel is applied to this copy. This type of matrix possesses a smoothing or blurring effect. But, for its purpose here, it is more appropriate to refer to the Gaussian kernel as a low pass filter. The application of the matrix blurs the small objects (i.e., particles) out of the image completely. However, the larger objects, i.e., bubbles, remain visible. For larger dimensions of the Gaussian kernel, larger objects can be smoothed from the image. Since a 9x9 matrix is the largest kernel that DaVis can apply, two successive Gaussian filters are applied to the TFPIV images. This provides sufficient smoothing to eliminate all particles from the images.

Background Intensity Correction - The negative of the image is then added to the original. The large objects appear as dark spots in the negative image that possess very low intensity values. The remaining bright portions of the image, including where the small objects were smoothed out, possess medium to high intensity values. Hence, the addition of the negative image intensifies the image excluding the pixels that are a part of the large objects. This step also proves advantageous to the application of TFPIV as it intensifies the particles relative to the background making them more distinguishable regardless of the background intensity or intensity gradients.

This image addition will usually include two constants that depend upon the particle-to-noise intensity ratio and the dynamic range of the image being processed (see

Figure 3.3). If a pixel in the blurred image is higher than in the original image, the pixel is set to zero intensity by the image subtraction. It is possible that the subtraction of the blurred image will eliminate particle images in this manner; therefore, a constant is subtracted from the blurred image prior to subtracting it from the original. The constant for this experiment was adjusted until the image addition was completed without the loss of particle images. Although not required, the second constant was added after the image subtraction to increase the ease of visual inspection during the performance evaluation of the processing algorithm. Only a small fraction of the particle images were lost throughout the variation of background intensities experienced in this experiment.

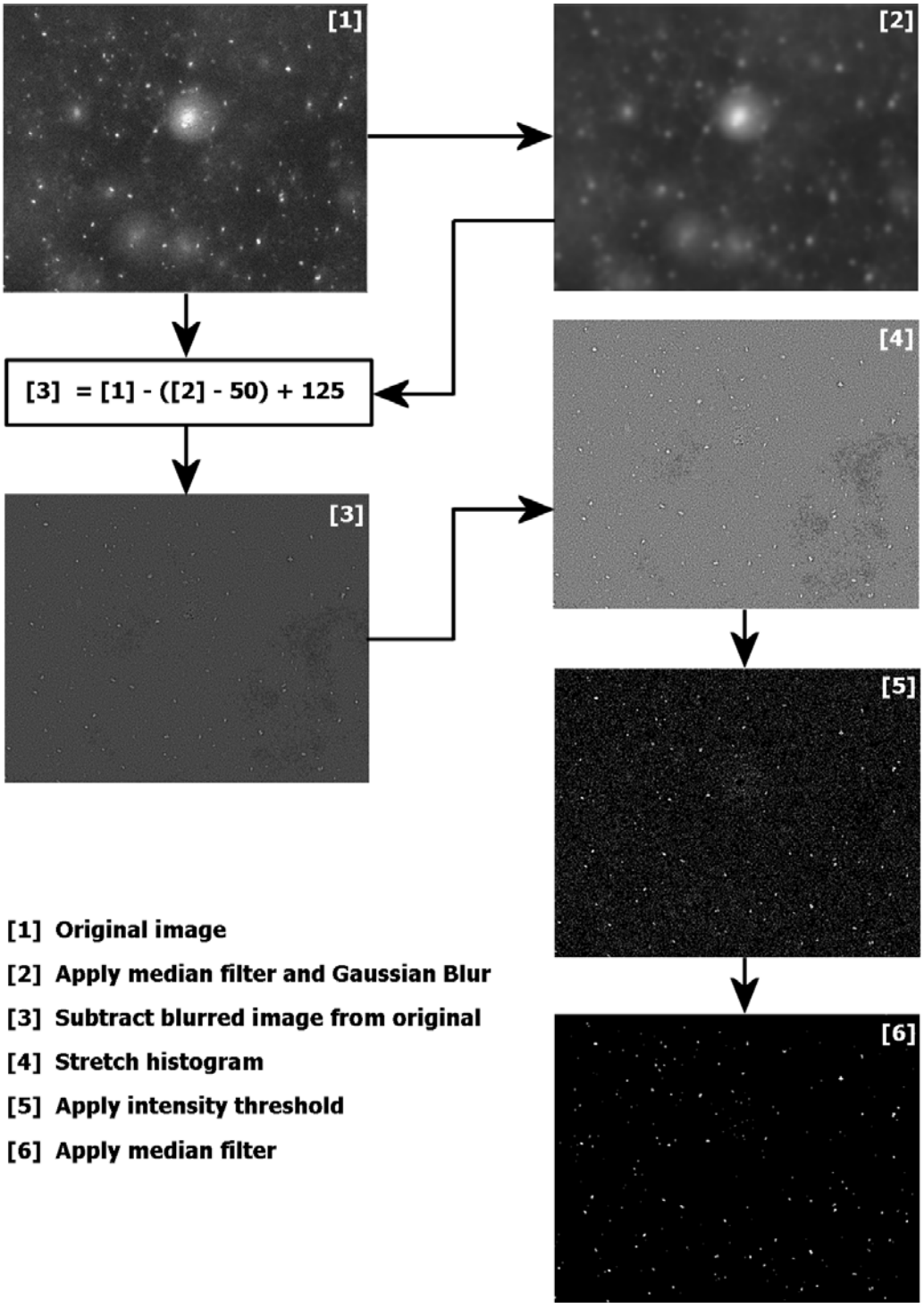

Figure 3.3 TFPIV image processing flowchart used for this experiment

Histogram Stretch – The addition of the negative Gaussian smoothed image not only eliminates the larger objects, but it also negatively affects the image by decreasing the range of intensities within the image. When the intensity histogram of the image is stretched, the contrast is increased and the objects in the image become more visible. This process, along with those preceding, also corrects for gradients in intensity due to the presence of ripples and disturbance waves. Ideally, the particles should now be the strongest signals in the image.

To stretch the histogram of an image, the standard deviation of the intensity, σ_o, is calculated. Then the deviation of each pixel intensity, I_o, from the average intensity, $I_{ave,o}$, is evaluated and is denoted by I_σ. Based on this deviation, each pixel is assigned a new intensity value, I_f, between the minimum and maximum possible values (0 and 255 for an 8-bit image). If the intensity of a pixel is above or below three standard deviations of the histogram, it is reassigned to the maximum $(I_{\max})$ or minimum $(I_{\min})$ intensity value of the new image respectively. If the intensity of a pixel is less than three standard deviations from the mean, it is reassigned to a linearly interpolated value between the minimum and maximum based on its deviation from the original mean intensity. This is done by calculating a new deviation, σ_f, for the adjusted minimum and maximum intensities.

$$I_\sigma = I_o - I_{ave,o} \qquad [3.3]$$

$$\sigma_f = \frac{\left(I_{\max} - I_{\min}\right)}{6} \qquad [3.4]$$

$$\begin{aligned} I_f &= I_{\min} && \text{if } I_\sigma < -3\sigma \\ I_f &= I_\sigma \frac{\sigma_f}{\sigma_o} && \text{if } -3\sigma_o < I_\sigma < 3\sigma_o \\ I_f &= I_{\max} && \text{if } I_\sigma > 3\sigma \end{aligned} \qquad [3.5]$$

Intensity Threshold – The last step of the image processing is to convert it to a binary image. This process also serves to eliminate any remaining low intensity traces of large objects. The value of the threshold limit must be determined by trial and error in order to prevent elimination of particles. The contrast of a particle with the background is dependant upon experiment-specific factors such as the laser incidence angle, the power of the laser, and the flow features present. A single threshold value can be found for all of the images that leaves the particle images while eliminating many of the interfacial reflections.

After these steps, additional median filters may be applied. However, these filters are more apt to eliminate particles from the image. This can occur as a result of the intensity threshold, which may eliminate lower intensity pixels that represent the edge of a particle. At this point in the image processing, particles may appear to be only one or two pixels.

With the application of these image processing steps, most complications that arise due to the presence of bubbles and interfacial features can be eliminated from the images. The complications presented by gas-liquid interfaces have prevented particle

image velocimetry from being utilized in thin films in the past. Therefore, the tuning of the image processing parameters, i.e., Gaussian radius, median filter size, and intensity threshold, are critical to the successful implementation of TFPIV.

3.6 Depth of Field Measurement

Typically, the depth of field for such experiments can be calculated via Equation [3.6] [Adrian, 1991] and Equation [3.7] utilized by Santiago et al. (1998) that employs the paraxial approximation: $NA = \sin\theta \approx \theta$.

$$\delta z = 4\left(1+\frac{1}{M}\right) f\#^2 \lambda \qquad [3.6]$$

$$f\#_p = \frac{1}{2NA} \qquad [3.7]$$

Depth of field is traditionally defined by the circle of least confusion for a particular camera and lens. The circle of least confusion is difficult to define, but is on the order of the Airy disc created by a slightly out-of-focus image point [Blaker, 1985]. Using the previous equations, the depth of field is calculated to be 9 microns for this system. However, this experiment does not possess the conventional definition of the depth of field. Rather, it is dependant upon the ability of the image processing techniques to eliminate out-of-focus particles.

To determine the depth of field that combines the optical and image processing factors, water droplets were taken from the flow loop reservoir and placed between two

glass microscope slides. A droplet had previously been placed on both slides, and the water was evaporated such that only the particles remained on the surface. Three small pieces of paper, acting as spacers, were placed between the outside edges of two slides creating a thin gap between them. The spacers created a gap between the slides approximately 100 microns wide, on the same order as the liquid film thickness. The slides were then positioned over the spacers with the dried particles facing inward. These steps were taken to correctly simulate the liquid film, and typical background intensities seen in experiments.

To measure the depth of field, images were taken as the camera was incrementally stepped towards the microscope slides. The images were processed using the image postprocessing technique described in Section 3.5. The final images show how the particle images are treated by the image processing algorithm as they are incrementally moved in and out of focus. Particles on the wall of the near slide were monitored as the images were processed. For these three particles the depth of field ranged between 55 and 60 microns: much larger than the calculated depth of field. This means that the average velocities measured in this experiment are the average velocities for a liquid volume element with a 55 to 60 micron thickness. This relatively large depth of field also creates additional experimental error, particularly if the velocity profile is non-linear across the depth of field. This subject will be further discussed in Section 4.1.1.

3.7 Vector Calculation & Processing

To calculate the velocity field of the flow, particle image velocimetry divides the images into interrogation areas. The coinciding interrogation areas within the image pair are then statistically correlated, producing a Fourier transform of the correlation (see Figure 3.4). The peaks in the correlation represent the interrogation window offset between the two images in the pair. Depending upon the experimental setup and application, more than one displacement peak may exist. They are produced by velocity gradients within the interrogation area, loss of pairs, or image noise. The offset represented by the highest peak is chosen as the velocity vector for this interrogation area.

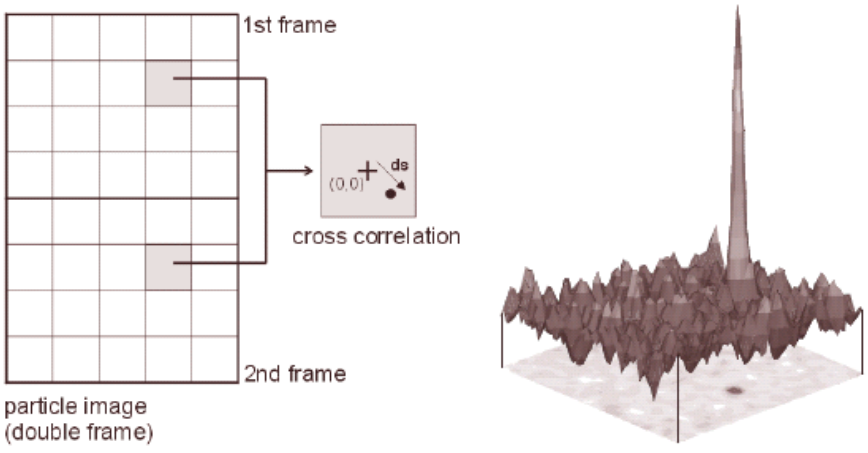

a) *b)*

Figure 3.4 PIV vector processing: a) dividing images into interrogation regions, b) typical displacement correlation of an interrogation region (LaVision GmbH, 2002)

The correlations, in addition to the other vector calculation methods and filtering, were completed through DaVis. The settings in this software allowed for a sophisticated flow analysis tailored to this particular experiment. Although the normalized correlation usually performs better in PIV analyses, it correlates both the particles in an interrogation area and the lack thereof. The regions of the images that originally possessed bubbles are represented as zero-intensity areas in the processed image void of any particles. To prevent the bubbles from affecting the vector calculations, the standard correlation function was applied rather than the normalized function. Since many micro-PIV experiments possess a depth of field thinner than the region of illuminated particles, Olsen and Adrian (2000) proposed a weighting function to be applied the correlation to minimize the effect of out of focus particles on the calculated vectors. However, the thorough image processing necessary for TFPIV disallows the utilization of this weighting function.

When interrogating a PIV image, it is important to take into account the susceptibility of the specific experiment to the loss of pairs. Both high velocity gradients within an interrogation region and out of plane motion can cause a particle to appear in only one of the coinciding interrogation regions of an image pair. The interrogation of these images is also affected by out of plane motions, such as when ripples or waves cause sudden radial motion in the film.

Although the turbulent scales and exact velocity profile within the liquid film are not known, the loss of pairs due to velocity gradients can be minimized via the adaptive

multi-pass interrogation method. The image pair is first evaluated with 256x256 pixel interrogation areas. The vectors for this pass are then used as the best guess values for a reduced grid of 128x128 pixels. After one more pass, the final interrogation grid is correlated at 64x64 pixels. The vector calculated in the previous pass is used as the initial guess for the next. This method increases the resolution of the vector field while reducing the number of uncorrelated particles. The interrogation regions also possess a 50% overlap to further reduce loss of pairs and create a smoother vector field. By reducing the number of uncorrelated particles, the multi-pass interrogation method increases the strength of the correlation peaks and decreases the possibility of false vectors.

During the interrogation process, the correlation peaks are evaluated after each pass to minimize the amount of false vectors. This is accomplished by applying three filters. The first checks to make sure that the interrogation area possesses at least three neighboring areas that have acceptable correlation peaks. The second eliminates each region that possesses less than a specified number of correlated pairs from the field. A value of seven is typically used to ensure a reliable vector calculation as shown in Figure 3.5 [Adrian, 1991]. However, this experiment is particularly subject to loss of pairs from out of plane motion, so this value was increased to ten correlated pairs for these measurements. The third filter compares the ratio of the two strongest correlation peaks, Q, within the interrogation area. If the ratio is not large, $Q < 3$, the vector is removed from the image. However, if the interrogation region possesses a $Q < 1.5$, it is replaced

with the second strongest peak. This peak evaluation continues through the fourth correlation peak until a peak with an acceptable ratio is found. The limits of *Q* used in this experiment were suggested values from the DaVis software manual.

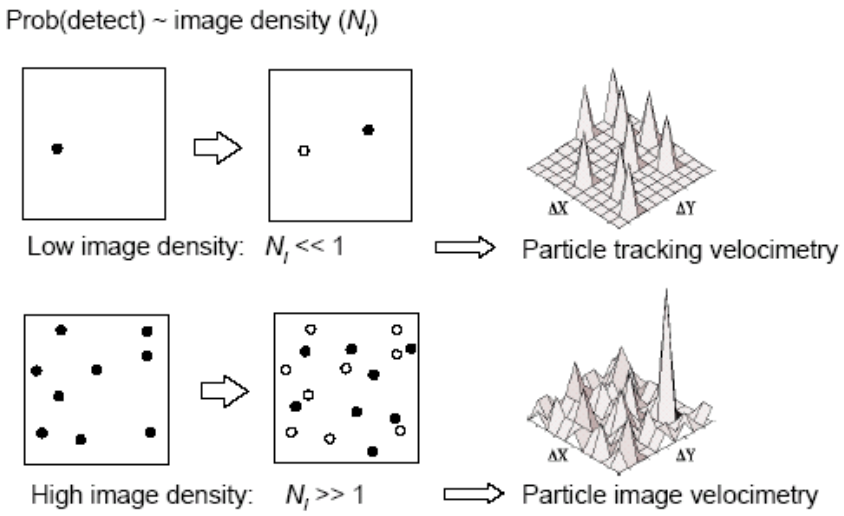

Figure 3.5 Importance of the image density, N_I, on the strength of the correlation peak (LaVision GmbH, 2002)

To further increase the accuracy of the velocity vectors, each pass in the multi-pass process can be iterated. Utilizing more than one iteration per pass can prove particularly beneficial when dealing with noisy images. However, with the addition of iterations, the computation time also increases. In addition, the extensive image processing may lead to the creation of false particles or the loss of actual particles. For this reason, two iterations were used for the first and second passes, while the last pass used only one.

3.8 Limitations of Image Processing for TFPIV

It is important to understand the limitations of the image processing techniques, particularly the algorithm utilized in this analysis. For this experiment, the process did eliminate real particles from the image and false particles were created. Varying the user-defined constants in each step will affect the noise within the image. Unfortunately, since the average image intensity varies drastically, a universal image processing algorithm will not remove all image noise without eliminating a significant number of particle images. Since particle concentration is the limiting factor in measurement resolution for thin films, the image processing was conducted in a manner such that particle images pass through along with image noise.

While the Gaussian blur and subtraction steps do remove large objects from the image, it is does not behave like the median filter. If the large objects in the image vary considerably in size, the Gaussian blur will not eliminate all traces of these objects. The range of unwanted objects ranged from large bubbles within the waves to out-of-focus particles. The application of a larger matrix will lead to a more effective removal of the unwanted objects. However, when the matrix is made larger, it will also increase the range of objects that will pass below this filter. Therefore, the application of multiple Gaussian blurs possessing different matrix sizes may eliminate the unwanted objects more effectively.

The median filter, as discussed in Section 3.6, can be used to limit the depth of field. To minimize the noise in the image, this filter should be applied multiple times during the processing as noise may be amplified during some of the processing steps. The median filter also serves to eliminate most of the coagulated particles on bubble surfaces.

Lastly, the intensity threshold is critical to the separation of the particles and image noise. Image noise is created in this experiment by dark noise, out-of-focus particles, and particles on the surfaces of bubbles. The dark noise is typically smaller and of lower intensity than the particle images in this experiment; therefore it is easily eliminated by the median filters and intensity threshold. However, out-of-focus particles introduced a fair amount of noise in this experiment since they possessed small groups of pixels near the same intensity as the particles. Since they are the same size as the particle images and near the same intensity, it is difficult to eliminate this type of noise. This task is even more difficult when the background intensity varies considerably.

The image processing applied in this TFPIV experiment allows the velocity data to be extracted successfully. It does extract the particle images from unwanted bubbles and varying background intensities, but not without the addition of false particles. The processed images, although much improved, still require careful interrogation and vector calculation.

4 TFPIV Measurements of Horizontal, Two-phase Flow

Data were collected for various flows within the wavy, wavy-annular, and annular regimes for the top, bottom, and side of the tube. Horizontal, annular, two-phase flow possesses waves and ripples that intermittently pass over the liquid film. In order to ensure valid time-averaged data, one hundred image pairs were collected for each flow setting at each camera position. The vector fields from this data allowed for the calculation of a time-averaged velocity and RMS velocity for the various flows. However, these average and RMS velocities do not represent that of the entire film. Rather, the data presented in this thesis are the averaged data for the volume element defined by the depth of field of the measurement system. Unless otherwise stated, the data were taken at approximately 75 microns from the wall with a depth of field of approximately 60 microns. This distance from the wall was chosen to maximize the particles within each image while maintaining the entire depth of field within the liquid film.

4.1 Average Liquid Film Velocity Profile

The velocity profile of the film is an important aspect of two-phase, annular flow heat transfer. Knowledge of the liquid film velocity profile will better our understanding of the liquid film and its relationship with the waves and gaseous core at the interface. The understanding of these relationships may lead the improvement of the film distribution model, which can then be integrated into the pressure drop and heat transfer models for horizontal, annular two-phase flow.

Hewitt et al. (1990) used photochromic dye traces to measure the liquid film profile for a relatively thick film on the order of millimeters (Figure 4.1). They found it to be approximately linear across much of the film thickness. However, many models for heat transfer or pressure drop, such as Dobran (1982) and Owen and Hewitt (1987), assume the universal velocity profile for the film, which originated from turbulent boundary layers of single-phase pipe flows. Although Hewitt's experiment is on a much larger scale than the current experiment, the liquid films under examination may possess similar profiles. The following velocity profile measurements will allow for the integration of the correct profile into the film distribution model.

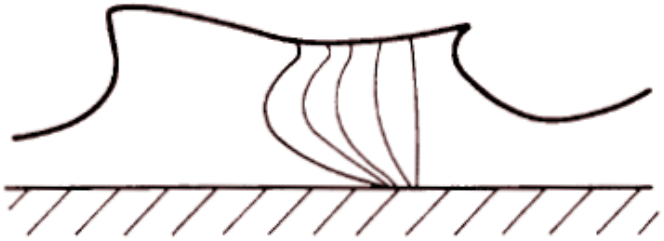

a)

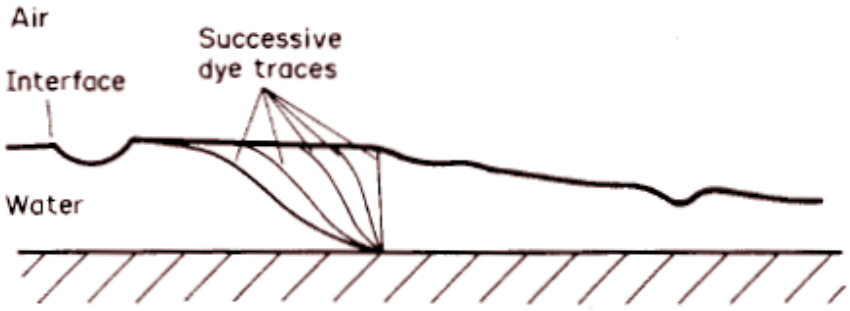

b)

Figure 4.1 Observed velocity profiles of thick liquid film in horizontal, two-phase flow (mean flow is from right to left): a) wave, b) base film (Hewitt et al., 1990)

4.1.1 Measurement and Analysis

Utilizing the same stepping method used for the verification of the particle distribution throughout the liquid film (Section 3.2.2), velocity vector fields were calculated for one hundred image pairs at multiple positions throughout the film thickness at the bottom, side, and top of the tube. For this analysis, the image processing settings were adjusted so the depth of field was approximately 30 microns. Because the spacing of the data points in these profiles is not particularly fine relative to the large velocity

gradients, error can be introduced by any gradients in the shear within the depth of field (see Figure 4.2). Curves in the velocity profile would prevent the average measured velocity from occurring at the plane of focus. However, it is unlikely that an inflection point or a region of zero-shear is present within the average film velocity profile; therefore, a linear approximation between points can be made with some confidence. Nonetheless, the most accurate velocity profile is measured when the depth of field is minimized.

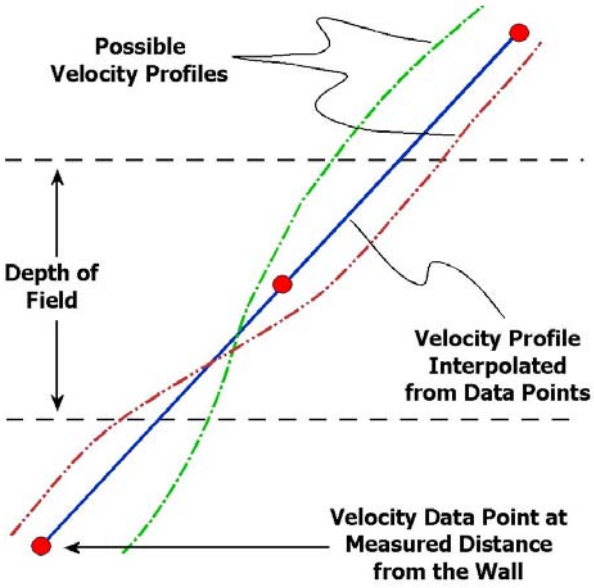

Figure 4.2 Potential velocity profile error induced by profile curvature within the depth of field

A wavy-annular flow with a relatively high liquid flow rate was evaluated for this measurement. This ensured a varying, but relatively thick, film around the tube's circumference. The first data points were taken fifteen microns from the tube wall: this

was the closest distance to the wall where particles consistently appeared throughout the TFPIV images. The micrometer stage was then used to step through the film until extending beyond the average film thickness. The majority of images at this distance are characterized by large areas that contain only out-of-focus particles. It is not uncommon for entire images to possess only out-of-focus particles at this distance from the wall.

These velocity profiles were then converted into dimensionless units using the friction pressure drop correlation of Müller-Steinhagen and Heck (1986) as presented by Ould Didi et al. (2002). The frictional pressure drop, $\left(\frac{dp}{dz}\right)_{friction}$, is essentially based on the phase mass fluxes and mass quality, and is related to the dimensionless units by the following equations.

$$\tau = \frac{d}{4}\left(\frac{dp}{dz}\right)_{friction} \quad [4.1]$$

$$u_\tau = \sqrt{\frac{\tau}{\rho_l}} \quad [4.2]$$

$$u^+ = \frac{u}{u_\tau} \quad [4.3]$$

$$y^+ = y\frac{u_\tau}{\upsilon_l} \quad [4.4]$$

In these equations, τ is the average shear stress in the film, d is the tube diameter, u_τ is the friction velocity of the film, and y is the distance from the tube wall. The measured liquid film velocity profiles are plotted over the dimensionless velocity, u^+, and the

dimensionless distance from the wall, y^+. The universal velocity profile, the liquid film profile assumed in the most accurate pressure drop and heat transfer models for air/water flow, is also shown on the plots. In these models, the velocity profile is assumed to be the same around the circumference of the tube. The following equations are used to describe a three-layer, universal turbulent profile shown [See Whalley, 1987, for example].

$$\begin{array}{lll} \text{viscous sub-layer:} & u^+ = y^+ & \text{for} \quad y^+ < 5 \\ \text{buffer layer:} & u^+ = -3.05 + 5\ln y^+ & \text{for} \quad 5 < y^+ < 30 \\ \text{inertial sub-range:} & u^+ = 5.5 + 2.5\ln y^+ & \text{for} \quad y^+ > 30 \end{array} \qquad [4.5]$$

4.1.2 Measured Velocity Profiles

The advantage of observing a wavy-annular film for this analysis is the effect of the flow's asymmetric film thickness. The differences in film thickness with circumferential position appear to affect the average velocity profiles of the liquid film. As can be seen from the data presented in Figures 4.3-4.6, the bottom, side and top velocity profile measurements produced different results.

The average bottom velocity profile appears to have a similar shape to that of a single phase, turbulent boundary layer. The film thickness at this position is approximately 450 microns. As will be seen in all of the measured velocity profiles, there is a significant difference between the shear between the data points at 15 and 65 microns compared to the shear between the neighboring points. However, the shear

between the wall and 15 microns and the shear between 65 and 115 microns are very similar.

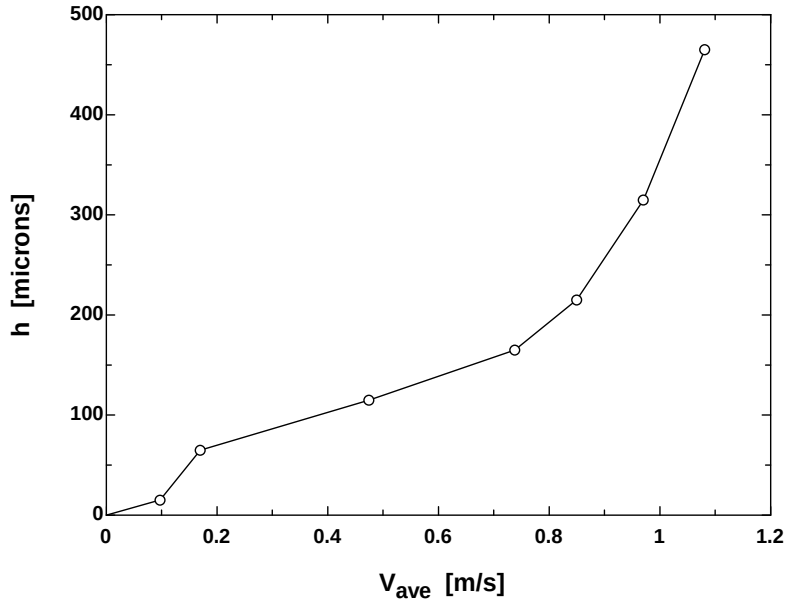

Figure 4.3 Liquid film velocity profile at the bottom of the tube

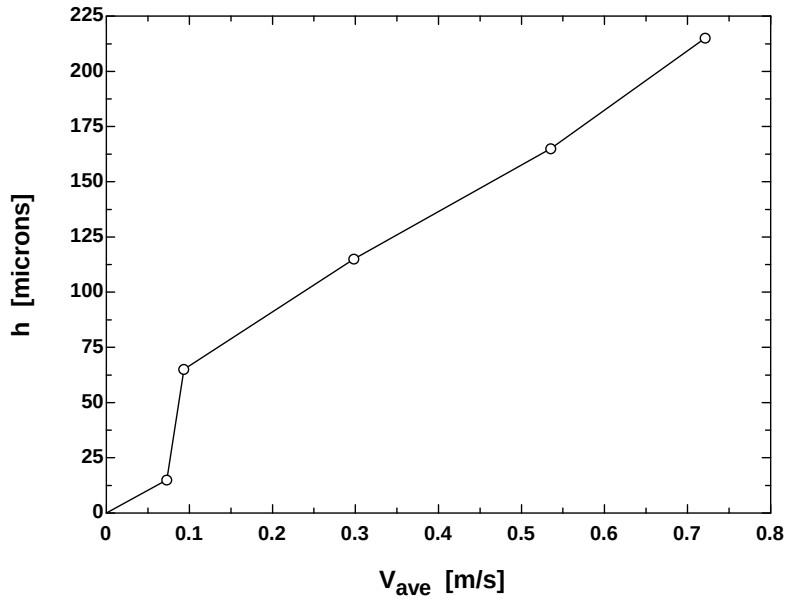

Figure 4.4 Liquid film velocity profile at the side of the tube

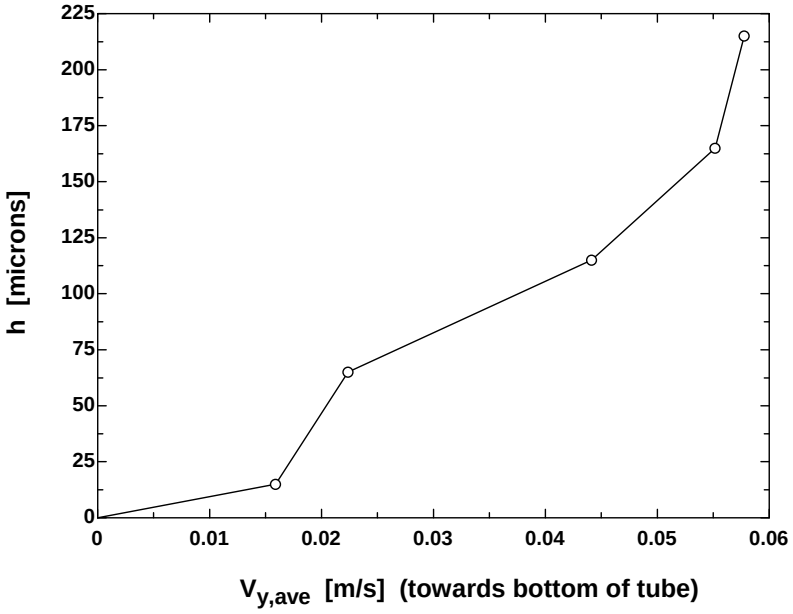

a)

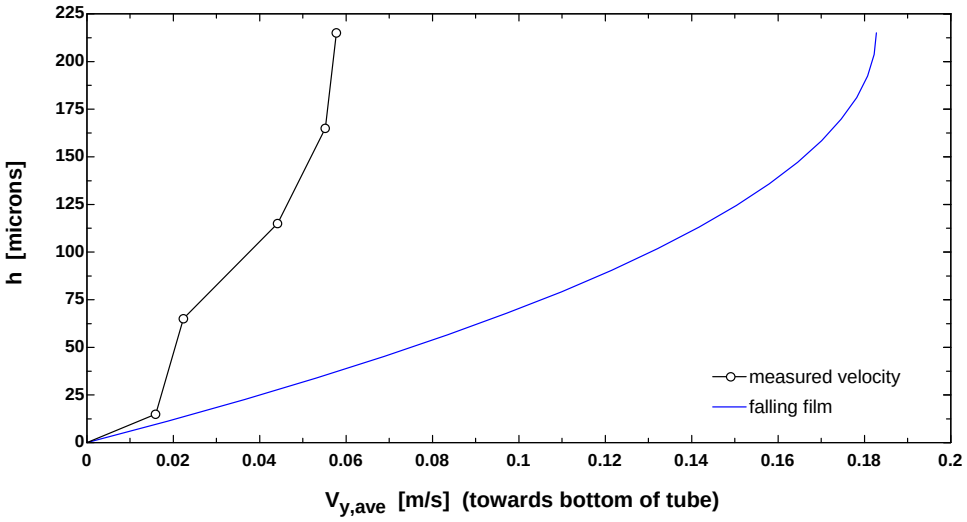

b)

Figure 4.5 Circumferential liquid velocity profile at the side of the tube a), and b) compared to falling film velocity profile derived from Navier-Stokes equation

At the side of the tube, the velocities demonstrated a comparatively linear profile; however, a drastic change in shear is present between 15 and 65 microns from the wall (see Figure 4.4). As is the case in the bottom velocity profile, the shear before and after these points matches fairly well. At the side position, the thinning film thickness, approximately 200 microns, has resulted in a change in the interfacial shear from the film velocity profile at the bottom of the tube.

The circumferential velocity profile at the side of the tube is plotted in Figure 4.5. Except for the change in shear in the region between 15 and 65 microns, the profile is similar to that of a laminar, gravity driven flow down a vertical surface as predicted by the Navier-Stokes equation. Although the magnitude of the measured profile is significantly smaller, the wall shear for both profiles is fairly similar.

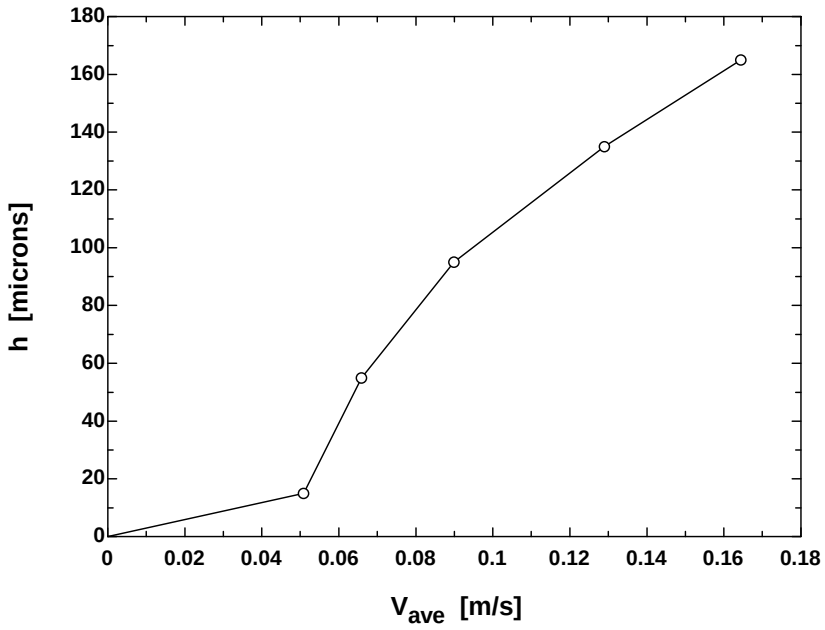

Figure 4.6 Liquid film velocity profile at the top of the tube

The average velocity profile at the top of the tube is not linear and has a curvature opposite to that of the universal profile. Again, the film is even thinner at this position, estimated to be near 150 microns based on the images beyond this distance from the wall. The shear gradually increases towards the air-water interface. The shear at the wall is much higher than that throughout the thickness of the film. It is also important to note that, unlike the side and bottom profiles, the shear beyond 15 microns from the wall appears to be fairly continuous.

4.1.3 Velocity Profile Comparison

As seen in Figure 4.7, the behavior of the liquid film varies considerably around the circumference of the tube. Because these measurements were made on a flow within the wavy-annular regime, the liquid film at the top, side, and bottom of the tube are subject to different flow mechanisms. The most obvious difference between the profiles is the decreasing film thickness from the bottom to the top of the tube. When comparing the profiles, one should also note that the wave height also decreases towards the top of the tube. Therefore, the waves will have a smaller effect on the film at the top of the tube. Lastly, gravity affects the film at each position differently. The factors that affect the profile at each position differently result in varying film velocity profiles around the circumference of the tube.

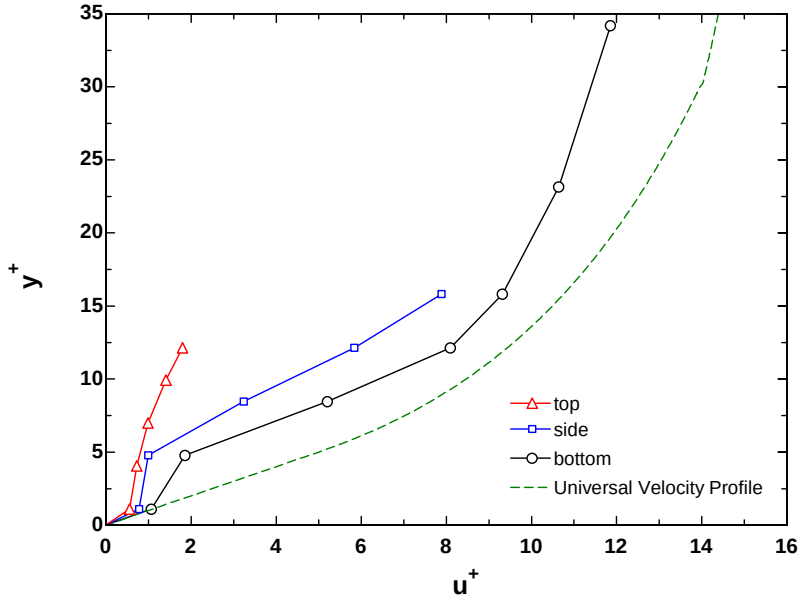

a)

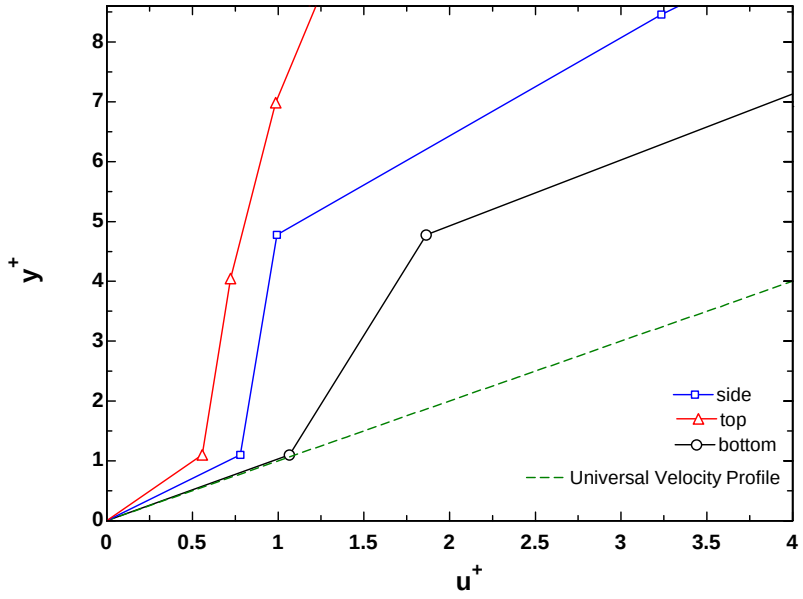

b)

Figure 4.7 Comparison of liquid film velocity profiles to the universal velocity profile in dimensionless units: a) overall profile, b) wall shear

The film velocity profile at the bottom of the tube appears to match very well with universal velocity profile as utilized in the pressure drop model by Ould Didi et al. (2002). The measured shear at the tube wall matches that predicted by the model nearly identically, and the velocity profile beyond 65 microns from the wall virtually parallels the universal velocity profile.

Although the velocity profile at the side of the tube is fairly linear beyond 65 microns from the wall, it does possess a similar shear to that of the universal velocity profile. The side velocity profile is fairly linear; however, because the profile only ranges from $y^+ = 0$ to $y^+ \approx 15$, it nearly parallels the universal velocity profile.

The liquid film at the top of the tube exhibits a much different behavior. It does not possess any of the characteristics of a turbulent boundary layer. The change in the film's behavior is most likely due to the factors discussed previously.

4.1.4 Wall Shear

Another important trend is the decreasing wall shear from the bottom of the tube to the top (Figure 4.7). As discussed in Section 4.1.1, the universal velocity profile is used to calculate the frictional pressure drop in the tube. For the flow examined in these profile measurements, the model predicts a pressure drop 20.2% higher than the measured value (Figure 4.8).

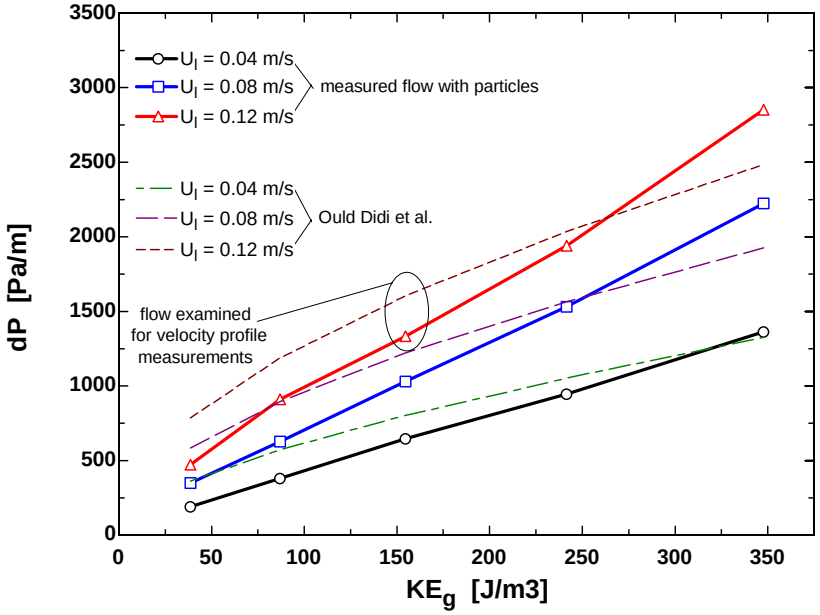

Figure 4.8 Measured pressure drop vs. the Ould Didi et al. (2002) model

The Ould Didi model predicted a significantly higher pressure drop than was measured. As previously mentioned, these models are typically a simplification of the physics of the flow. Therefore, to validate the measured shear at the tube wall, it is more appropriate to compare the measured wall shear to the pressure drop within the tube using the following equations:

$$\frac{\partial u}{\partial y} = \frac{1}{3}\left(\left.\frac{\partial u}{\partial y}\right|_{bottom} + \left.\frac{\partial u}{\partial y}\right|_{side} + \left.\frac{\partial u}{\partial y}\right|_{top} \right) \qquad [4.6]$$

$$\tau_{wall} = \mu_l \left(\frac{\partial u}{\partial y} \right)^2 \qquad [4.7]$$

$$\tau_{wall} P_{tube} = A_c \left. \frac{dp}{dz} \right|_{friction} \qquad [4.8]$$

The velocity gradient at the wall, $\frac{\partial u}{\partial y}$, is calculated by averaging the velocity gradients at the bottom, side, and top of the tube. These velocity gradients at the wall for the three measurement positions were assumed to be the change in velocity from the wall to the first data point, i.e., 15 microns from the wall. The viscous wall shear, τ_{wall}, is then calculated using the liquid viscosity, μ_l. A frictional pressure drop, $\left. \frac{dp}{dz} \right|_{friction}$, is calculated in Equation [4.8] from the wall shear through a relation with the tube perimeter, P_{tube}, and the tube cross sectional area, A_c.

The frictional pressure drop calculated from these relations is 20.7% smaller than the measured pressure drop shown in Figure 4.8. This suggests that approximately 80% of the pressure drop in horizontal, annular two-phase tube can be attributed to friction at the wall. The remaining pressure drop could be due to gas-liquid interaction such as wave formation and droplet entrainment.

4.1.5 Near-wall Velocity Profile

The variation in shear between 15 and 65 microns in the bottom and side velocity profiles is unlike that of single phase, near-wall profiles. It is difficult to explain why this flow deviates from the universal velocity profile, which predicts constant shear stress

below $y^+ = 5$. One possible explanation is that measurements within this distance from the wall are rare for turbulent flows. However, Khoo et al. (2001) conducted hot-wire measurements down to $y^+ \approx 2$, and Nowak (2002) measured the turbulent boundary layer profile from $y^+ \approx 1.5$ utilizing ultrasound Doppler velocimetry. Neither of these experiments produced results deviating from a near-constant shear in the viscous sub-layer.

A more likely explanation can be found when considering the liquid film in horizontal, annular two-phase flow as a highly transient flow. For example, waves accelerate the film as they pass through, while the film decelerates and, in the case of the top and side film, drain towards the bottom between the waves. The waves also affect the gas flow that is dragging the liquid film along the tubes. As shown by Hagiwara et al. (1989), the gas accelerates above the mean gas velocity as it passes over the crest of the wave. After it passes over the crest, the gas quickly decelerates below the mean gas velocity, but gradually increases towards the mean.

When considering the varying interfacial forces on the liquid film from the waves and gas flow, it becomes apparent how drastically and quickly the liquid film velocity profile could change with time. The liquid film directly behind a wave is moving at a relatively high velocity with a high velocity gas flowing over it. The liquid film is slowest directly in front of the wave with a relatively low velocity gas flowing over it. Therefore, to understand the near-wall velocity profile, experiments or modeling should

be conducted to monitor the penetration depth of these interfacial forces, along with the speed at which this penetration depth propagates through the film towards the tube wall.

This experiment could be very similar to the flow simulated by Fukano and Inatomi (2003). The experiment would be initialized when a gas flow is applied over a stagnant, stratified liquid. The development of the two-phase flow could be monitored. A high speed camera could be used to take quick, successive images of the film, thus monitoring the velocity profile of the film via PIV, or photochromic dye activation, for example.

4.2 Time-Averaged Liquid Film Velocity Measurements

As was done in the BST analysis (Chapter 2), the TFPIV method was used to calculate the average axial and circumferential liquid film velocities for various flow settings within the wavy, wavy-annular, and annular regimes. This will also serve as a verification of the bubble streak tracking method's accuracy. However, the analysis with the TFPIV is limited to two important trends noted within the BST data: the variation of the average axial liquid film velocity around the circumference of the tube, and the average circumferential liquid film velocities at the side of the tube for varying flow rates. One should also note that the average velocities discussed here are the average velocities for the liquid film within the depth of field.

4.2.1 Time-Averaged Axial Liquid Film Velocity

The average axial liquid velocities for multiple flow rates are plotted in Figure 4.9. The average axial velocity increases with increasing superficial gas velocity and superficial liquid velocity. As the curves approach the annular regime, the superficial gas velocity has a decreasing effect on the average liquid film velocity. This suggests that gas velocity, or interfacial shear, has a decreasing effect on the average film velocity in annular flows. In Figure 4.9a, the liquid film is becoming more evenly distributed about the tube's circumference. Therefore, the data imply that the average axial film velocity may be correlated to the liquid film thickness for horizontal, wavy and wavy-annular flows.

The superficial liquid velocity demonstrates a somewhat linear relationship with the average axial liquid film velocity (Figure 4.9b). As the mass of liquid within the tube increases, the average axial velocity linearly increases with a slope defined by the gas velocity. Although more data points are required to verify such a relationship, the film thickness, which is associated with the superficial liquid velocity, appears to be related to the average axial liquid film velocity.

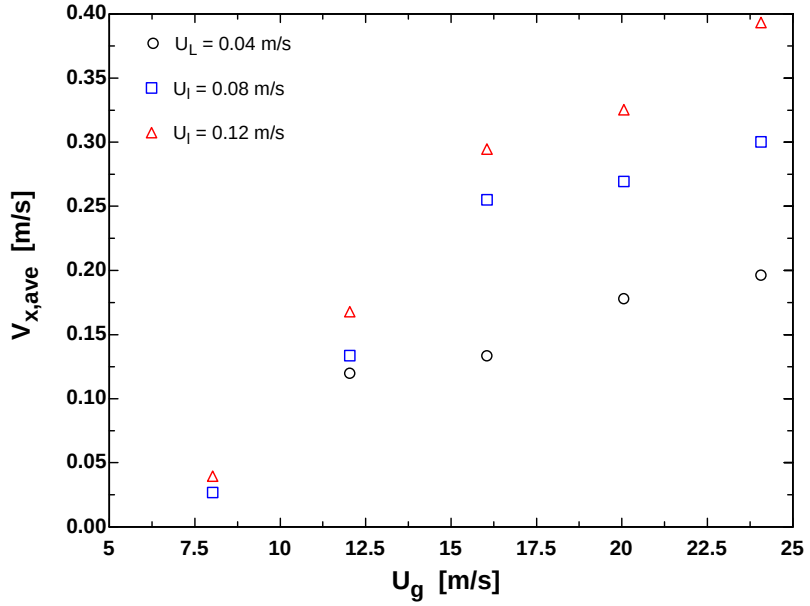

a)

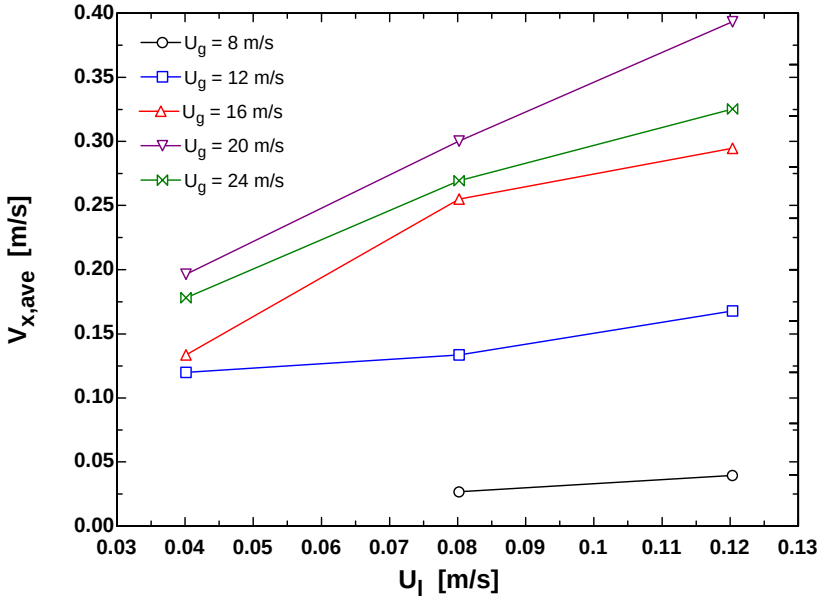

b)

Figure 4.9 Average axial liquid velocity at the side of the tube vs. a) superficial gas velocity and b) superficial liquid velocity

4.2.2 Time-Averaged Circumferential Liquid Film Velocity

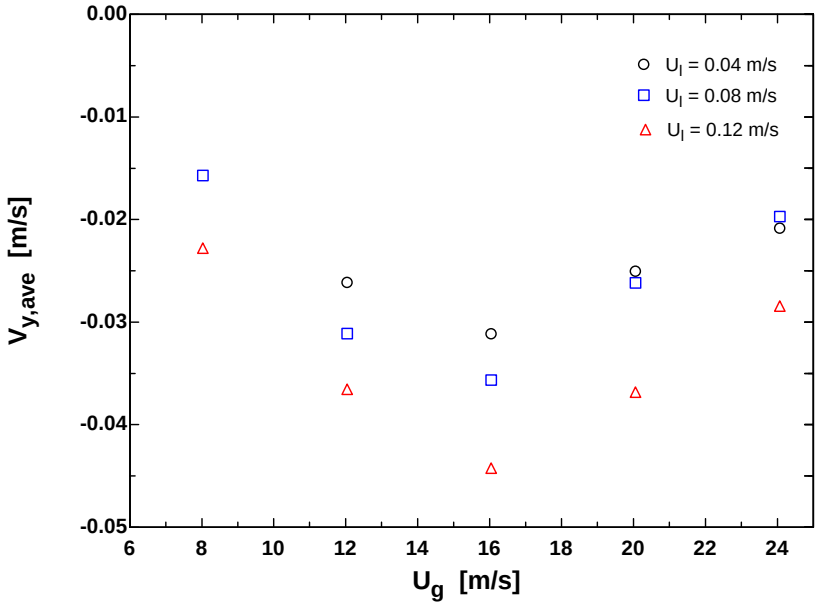

Figure 4.10 Average circumferential velocity at the side of the tube vs. superficial gas velocity

The circumferential velocity at the side of the tube appears to correlate well with superficial gas velocity (Figure 4.10). The lowest superficial gas velocity flow produces a wavy flow where waves intermittently push liquid onto the sides of the tube. For these flows, the film is, on the average, very thin on the sides of the tube. The velocities at these wavy flows are most likely dependant upon the wettability of the tube material. If the tube material has a high wettability, the fluid will flow down the tube walls more slowly. As the gas velocity is increased, more liquid is pushed up the sides of the tube causing an increase in film thickness. Since more liquid is present on the tube walls, the

effect of the material wettability decreases and the film flows down the wall at an increased rate.

As the flow reaches the wavy-annular regime, $U_g \approx 16$ m/s, the magnitude of the circumferential velocity reaches its peak. Beyond this point, the flow moves toward the annular regime and the circumferential velocity at the side of the tube decreases in magnitude. This indicates the effects of a more evenly distributed liquid film, the presence of a fluid mechanism that resists the liquid flow down the tube walls, or the combined effect of both.

One should also note the relationship between the superficial liquid velocity and the average circumferential velocity at the side of the tube. At $U_g = 12$ m/s, within the wavy regime, the difference between the circumferential velocities of the three superficial liquid velocities is nearly equal. However, as the flow moves into the annular regime, the magnitudes of the circumferential velocities at $U_l = 0.08$ m/s decrease relative to those at $U_l = 0.04$ m/s. This also suggests the existence of a mechanism resisting the flow down the tube. At the lowest superficial liquid velocity, the mechanism may have a lesser effect due to the high viscous shear through the thin film. However, the thick liquid film at the highest superficial liquid velocity may be decreasing the mechanism's effect on the circumferential velocity. The intermediate superficial liquid velocity possesses a film thickness between the other two data sets. This liquid velocity appears to balance the

viscous shear and film thickness effects to amplify the effect of this fluid mechanism on the circumferential liquid velocity.

4.2.3 Comparison to BTV Measurements

The TFPIV technique is more complex and expensive compared to BST, but the data are easier to extract. Therefore, statistically sound average velocities were acquired for the TFPIV experiment. If the measurement of the bubble streaks in the BST technique were automated, it would pose as a much more economical measurement method. To verify the BST results, they are compared to the TFPIV results. However, since the measurements were taken in different diameter tubes and the TFPIV measurements do not necessarily represent the average velocity of the overall film, only the trends of the data can be compared. BST requires entrained bubbles to exist within the film. As shown by Rodríguez and Shedd (2004), the bubbles are entrained by the waves in horizontal, two-phase annular flow. Because the liquid flow in the wavy regime is fairly smooth, and only intermittently disturbed by waves, the average bubble velocities in wavy flows will be biased to the images directly behind the waves where the bubble concentration is the highest. In addition, the liquid film in the wavy regime is very thin and its velocity appears to be dependant upon the wettability of the tube material, as previously discussed in Section 4.2.2. For these reasons, this comparison is also limited to the wavy-annular regime.

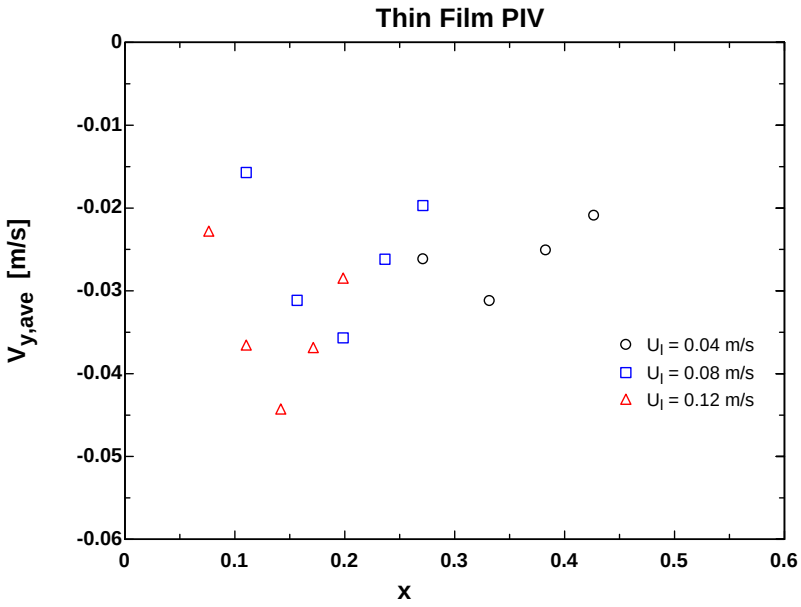

a)

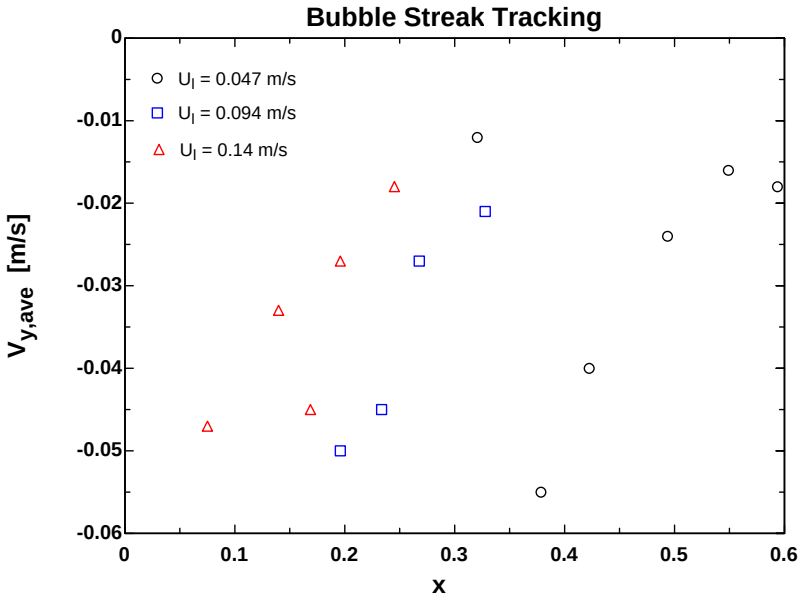

b)

Figure 4.11 Average circumferential liquid velocity measurements at the side of the tube vs. mass quality for a) TFPIV and b) BST

The TFPIV and BST circumferential velocity data at the side of the tube possess similar trends and values when plotted against mass quality, *x*. As seen in Figure 4.11, the magnitude of the circumferential velocity decreases as the flow moves through the wavy-annular regime for both data sets. However, the TFPIV data suggests that as the superficial liquid velocity increases, the magnitude of the circumferential velocity decreases. The BST data does not possess this trend; rather, it shows a slightly increasing velocity magnitude. These plots also demonstrate that the circumferential velocity at the side of the tube can be correlated with mass quality as well as superficial gas velocity.

The axial velocities on the side of the tube can also be compared for the two measurement techniques. The plots in Figure 4.12 show similar trends with increased mass quality. The measured axial velocities of the highest superficial liquid velocity are the most sensitive to a change in mass quality, while the lowest superficial liquid velocity is the least sensitive.

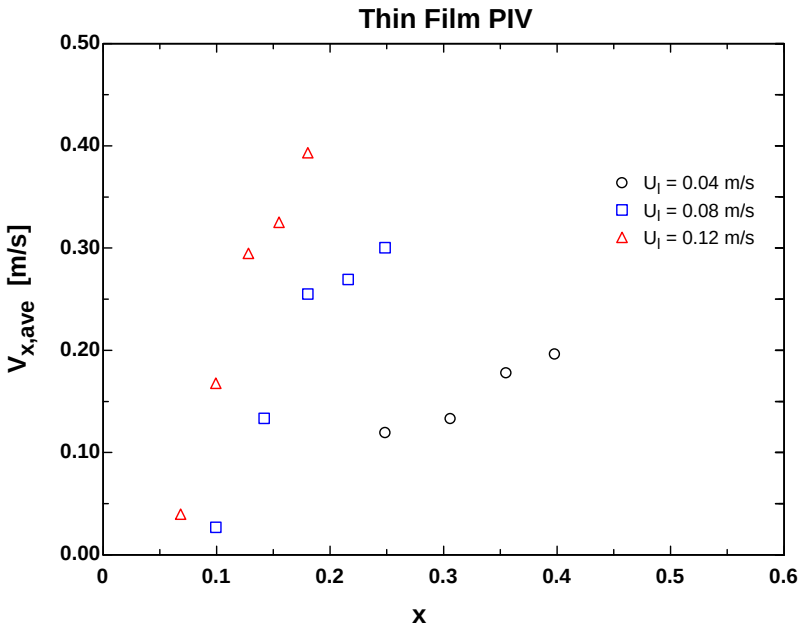

a)

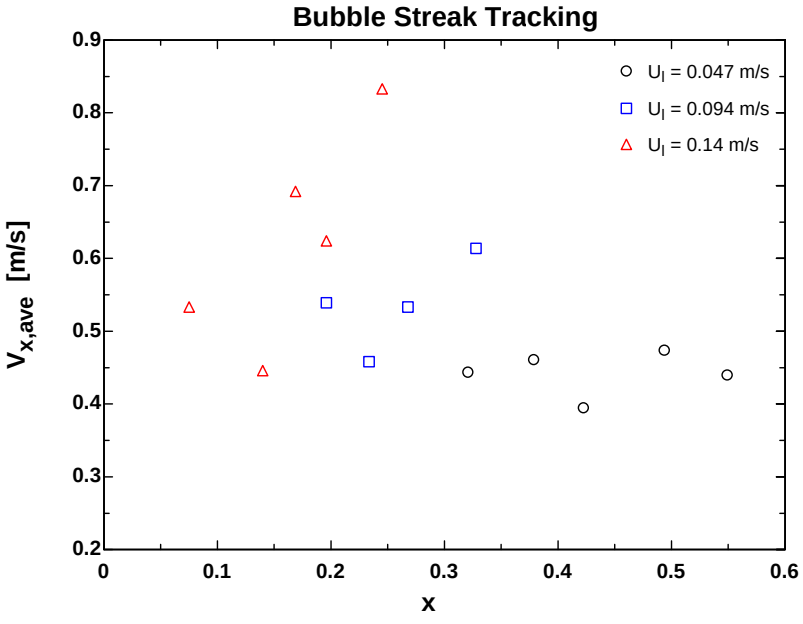

b)

Figure 4.12 Average axial liquid velocity measurements at the side of the tube vs. mass quality for a) TFPIV and b) BST

While the trends in the BST data are not as strong as those in the TFPIV data, both data sets exhibit similar behavior. The values of the axial velocity from the BST data are larger; however, this may be due to the radial position of the bubbles within the liquid film. From the TFPIV images, it appeared that the bubbles remained in the portion of the film closer to the interface, while the TFPIV data was collected at roughly half the film thickness. Acquiring more data will produce a sound statistical average that may reduce the variation in the BST data. This comparison has shown that the BST, along with non-trivial automation of the data processing, can provide a more economical alternative to TFPIV for the local liquid velocity measurement of thin films.

5 Qualitative Observations of Horizontal, Two-Phase Flow

The mechanisms within two-phase, annular flow have been studied for many years; however, they are still not well understood. As has been done with many complex flows, qualitative information has been gathered for these and similar flows in order to infer the physical behaviors that govern the fluid motions. Over the course of this study, a number of qualitative observations have been made that may lead to further understanding of these mechanisms. This section is dedicated to the discussion of these observations in order to assist further research of two-phase, annular flow.

5.1 Capillary Waves

It has been noted that within the BST and TFPIV images, the interfacial structures that have been described as ripples throughout this thesis as well as the literature, appear to be capillary waves. These waves are similar to those found in the ocean except that these ripples are flowing over a thin film. The nature of these ripples was discovered by observing the images taken beneath the ripples.

Several TFPIV images, particularly at the sides and top of the tube, exhibited a band of particles that moved opposite to the direction of the bulk flow. These bands have

been observed to be orientated anywhere from perpendicular to the bulk flow to nearly parallel; they are also characterized by a decreased number of particles. These traits are characteristic of capillary waves. The bands present within the TFPIV images are most likely the troughs of the capillary waves. Just as in typical energy waves, the fluid directly in front of the wave is drawn upwards as these capillary waves travel through a continuous fluid. Therefore, the waves are composed of a trough followed by a peak.

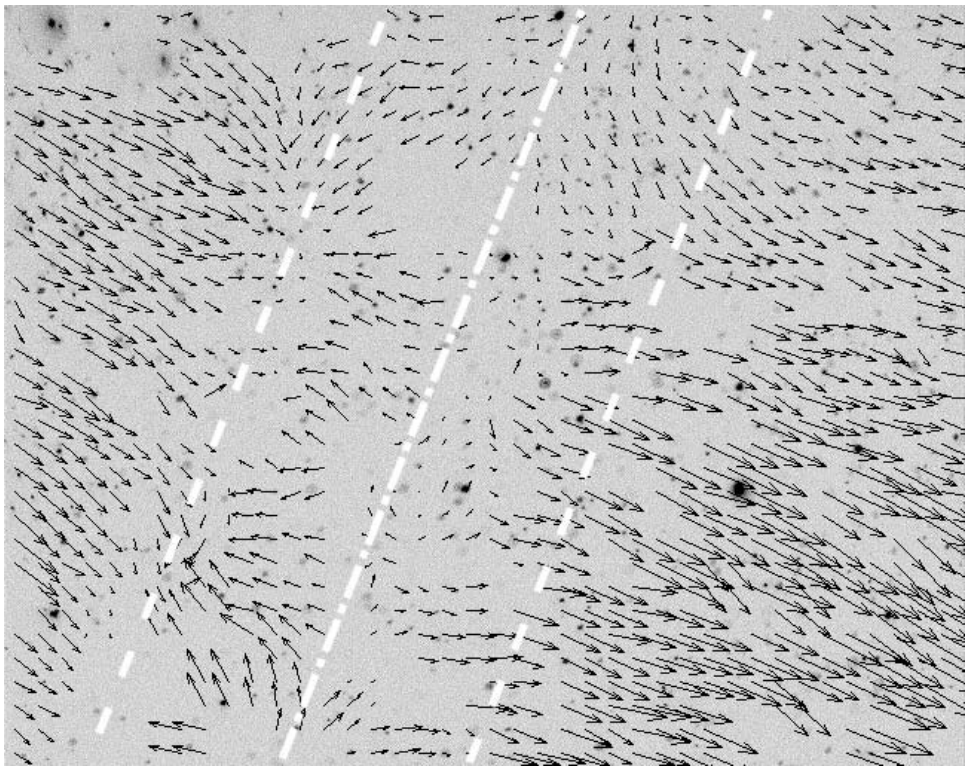

Figure 5.1 Capillary wave perpendicular to wavy-annular flow. Lines mark the ripple's wavelength and center peak (bulk flow from left to right)

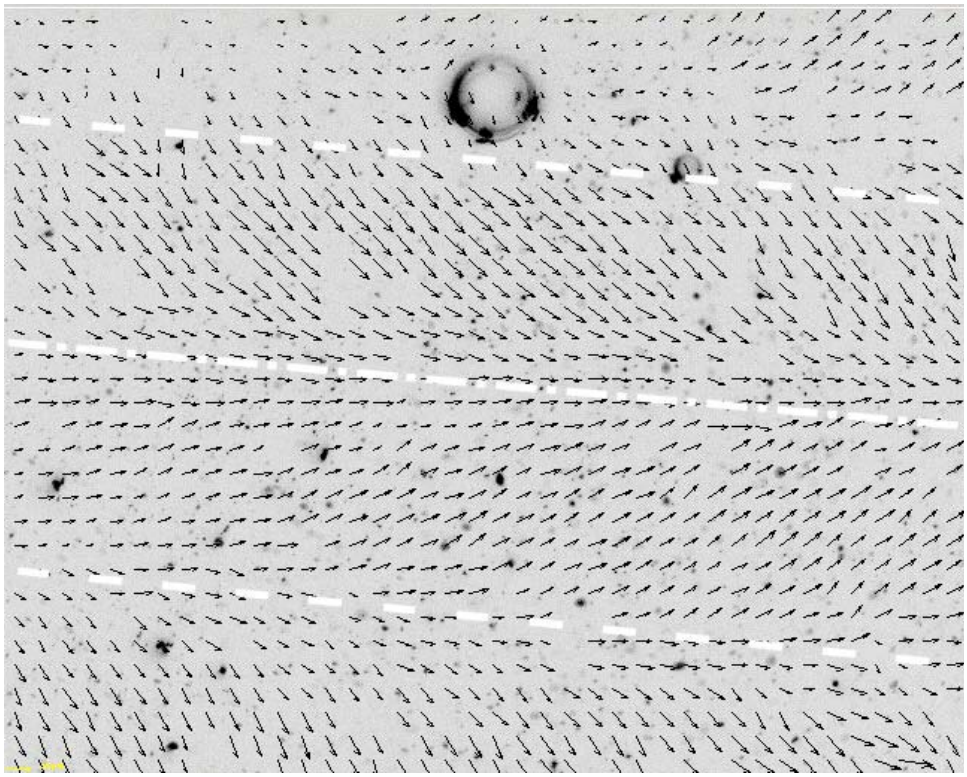

Figure 5.2 Capillary ripple parallel to wavy-annular flow. Lines mark the ripple's wavelength and center peak (bulk flow from left to right)

Capillary waves differ from gravity waves in the force that acts to restore them. Capillary waves typically possess a much smaller wavelength because surface tension, not gravity, is the primary restoring force. The wavelength at which the transition from gravity to capillary waves occurs, $\lambda_{\min}$, can be approximated by Equation [5.1] (see Kundu and Cohen, 2004). In this relation, σ is the liquid surface tension, ρ is the liquid density, and g is the gravitational force.

$$\lambda_{\min} = 2\pi\sqrt{\frac{\sigma}{\rho g}} \qquad [5.1]$$

For an air-water interface, λ_{min} is approximately 17.3 mm. The largest trough in the TFPIV experiment is less than 1.0 mm: much smaller than this transition value (see Figure 5.2). Due to the nature of the flow, it is also unlikely that a ripple with a wavelength greater than the image size could exist. With this information, along with the fact that gravity acts in the wrong direction to act as the restoring force on waves at the side or top of the tube, the ripples observed in both annular and wavy-annular flows can be treated as capillary waves.

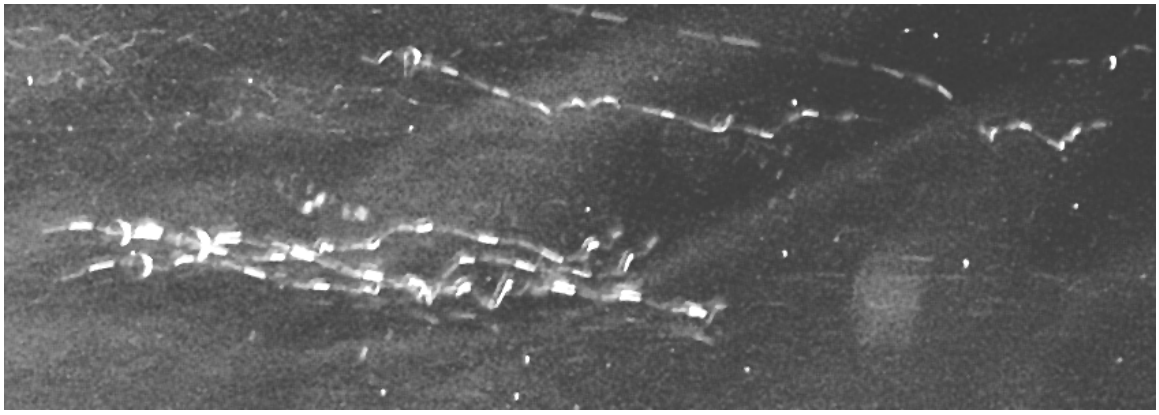

Figure 5.3 Bubble streaks in liquid film below capillary waves (bulk flow from right to left)

Bubble streaks have also suggested this type of motion within the liquid film (Figure 5.3). Throughout the BST images, some bubbles, which are traveling near the bulk film velocity, demonstrate a very strong deceleration followed by an equally strong acceleration to its original velocity. This type of motion is found near reflections from the air/water interface indicating the presence of ripples.

5.2 Wave Observations

Over the course of these experiments, the liquid film distribution mechanism has been closely examined. The BST and TFPIV data suggest that secondary flows and wave spreading are not the primary mechanism. The entrainment model employed in Section 2.6.3 suggests that droplet entrainment and deposition is not the primary mechanism either, at least not in the wavy-annular regime. As concluded in Chapter 2, the wave pumping mechanism requires a close examination because, in the author's opinion, the waves are responsible for distributing the liquid film.

The waves in the wavy-annular regime vary in amplitude. It is possible that relatively small waves were observed throughout the collection of the average film velocity data in Section 4.2. One of these potential waves is shown in Figure 5.4. One should note the slow, downward flow in front of the wave crest, and the strong, upward motion within the wave. The velocity vectors behind the wave are towards the top of the tube, but with decreasing amplitude. Further evidence that this may be a small scale wave is the difference between the calculated vectors, and those of the capillary waves shown in Figure 5.2.

Images from the BST experiments show that bubbles beneath the crests of waves have similar velocities to those exhibited in Figure 5.4. One of these images, shown in Figure 5.5a, show bubble streaks with a slow, downward motion directly in front of the wave front at the right. A relatively large bubble, which was within the wave crest when

the Xenon strobe flashed, exhibits a much faster velocity towards the top of the tube. The second image, Figure 5.5b, shows streaks from multiple bubbles in the upward direction.

These observations are meant to provoke further research of the waves within horizontal, annular two-phase flow. The strong, upward motions of these waves suggest that they play a significant role in the distribution of the liquid film.

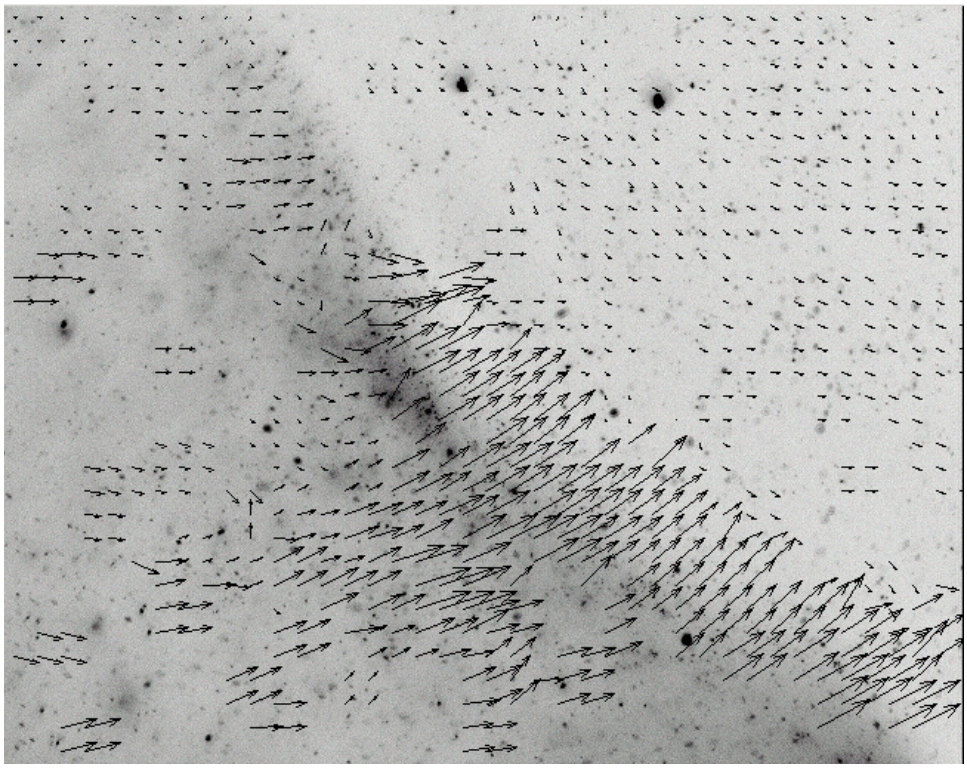

Figure 5.4 Small scale wave propagating up tube wall, negative image (bulk flow from left to right)

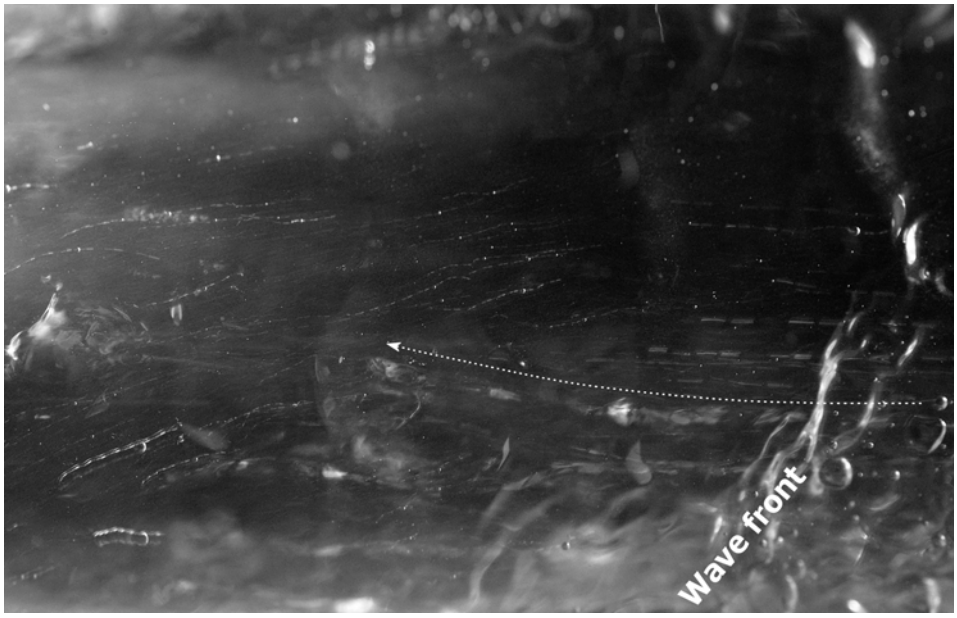

a)

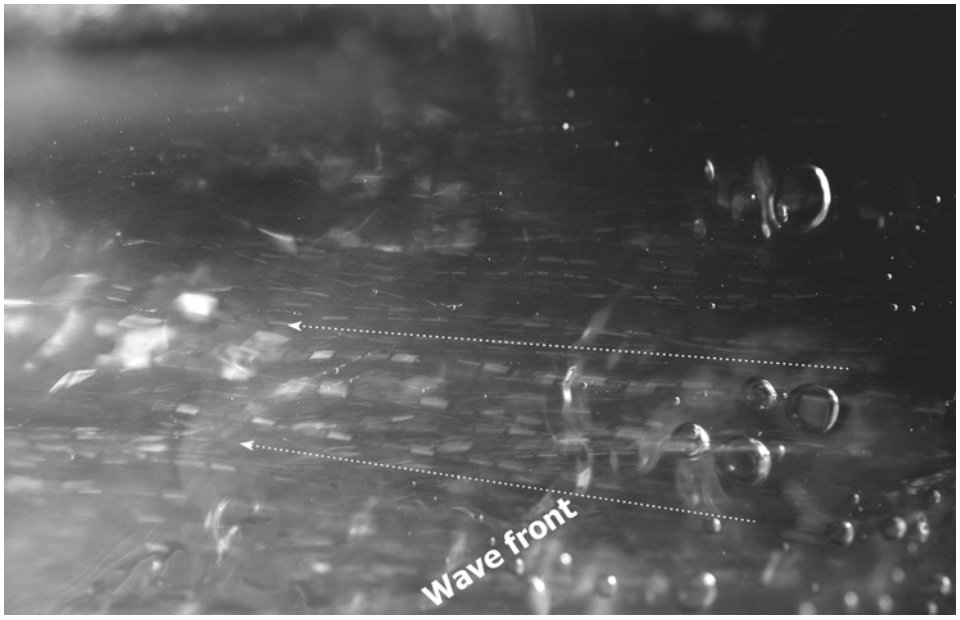

b)

Figure 5.5 Upward moving bubbles within the crest of a wave: bubbles leave streaks along the dotted line (height of picture is approximately the diameter of the tube, flow is from right to left)

6 Summary of Thesis

The Bubble Streak Tracking (BST) and Thin Film Particle Image Velocimetry (TFPIV) techniques have been proven as useful tools in the analysis of annular two-phase flow. These measurement techniques are presented as useful tools for examining the nature of the liquid film, with an ultimate goal of improving the pressure drop and heat transfer correlations for annular two-phase flow.

The techniques have been developed and applied to horizontal wavy, wavy-annular, and annular flows. Both techniques produced comparable average liquid film velocity data for the liquid film on the bottom, side, and top of the tube. This data has shown a net mass flux down the side of the tube, which does not support two of the four major proposed liquid film distribution mechanisms. The remaining two mechanisms cannot be directly analyzed with these methods; however, images acquired with both techniques suggest the waves play a significant role in the distribution of the liquid film.

Along with the average liquid film velocity measurements, the first measurement of the average liquid film velocity profile has been conducted with the TFPIV technique. The time-averaged film velocity profile at the bottom of the tube appears to match the universal velocity profile for a single phase turbulent boundary layer. The side profile is nearly linear, while the profile at the top of the tube is bent over in the direction of the bulk flow. These average profiles, however, differ from typical, single-phase velocity profiles in that they exhibit drastic changes in shear in the near-wall region. The reason

for this behavior is not determined in this thesis; however, it is most likely due to the highly transient nature of the liquid film in annular two-phase flow.

This thesis describes the measurement methods required to examine the nature of the liquid film in annular two-phase flow. The average film velocity measurements and observations made have increased our understanding of the characteristics of horizontal, two-phase flow as it transitions from wavy to annular. The average velocity profiles measured by the TFPIV method have provided valuable information regarding the liquid film. These measurements also demonstrate how TFPIV can be used to drastically increase the pressure drop and heat transfer models for annular, two-phase flow.

Bibliography

Adrian, R.J., 1991, "Particle-imaging techniques for experimental fluid mechanics," *Annual Review of Fluid Mechanics*, pp. 261-304.

Azzopardi, B.J., 1997, "Drops in Annular Two-Phase Flow," *International Journal of Multiphase Flow*, 23, pp. 1-53.

Azzopardi, B.J., Whalley, P.B., 1980, "Artificial Waves in Annular Two-Phase Flow," *Basic Mechanisms in Two-Phase Flow and Heat-Transfer*, pp. 1-8.

Bird, R.B., Stewart, W.E., Lightfoot, E.N., 2002, *Transport Phenomena*, John Wiley & Sons, Inc., New York, New York.

Blaker, A.A., 1985, *Applied Depth of Field*, Focal Press, Boston, Massachusetts.

Butterworth, D., Pulling, D.J., 1972, "A Visual Study of Mechanisms in Horizontal Annular Air-Water Flow," *UKAEA Report No. AERE-M2556*.

Chen, X.Q., Periera, J.C.F., 1999, "Two-way coupling: effects on two-phase flow predictions," within Celata, G.P., Di Marco, P., Shah, R.K., *Two-Phase Modeling and Experimentation 1999*, Vol. 3, pp. 1153-1160, Rome, Italy, May 1999. Edizioni ETS, Piza.

Choi, H.M., Kurihara, T., Monji, H., Matsui, G., 2001, "Measurement of particle/bubble motion and turbulence around it by hybrid PIV," *Flow Measurement and Instrumentation*, 12, pp. 421-428.

Clark, W.W., 2000, *The Interfacial Characteristics of Falling Film Reactors*, Chapter 6. Doctor of Philosophy Thesis, School of Chemical, Environmental, and Mining Engineering, University of Nottingham.

Cousins, L.B., Hewitt, G.F., 1968, "Liquid Phase Mass Transfer in Annular Two-Phase Flow: Droplet Deposition and Liquid Entrainment," *UKAEA Report No. AERE-R5657*.

Crowe, C.T., Troutt, T.R., Chung, J.N., 1996, "Numerical models for two-phase turbulent flows," *Annual Review of Fluid Mechanics*, 28, pp. 11-43.

Darling, R.S., McManus, H.N., 1968, "Flow Patterns in Circular Ducts with Circumferential Variation of Roughness: a Two-Phase Flow Analog," *Proceedings of the 11th Midwestern Mechanics Conference (Developments in Mechanics)*, 5:153-170.

Dobran, F., 1983, "Hydrodynamic and heat transfer analysis of two-phase annular flow with a new liquid model of turbulence," *International Journal of Heat and Mass Transfer*, 26, No. 8, pp. 1159-1171.

Driscoll, K.D., Sick, V., Gray, C., 2003, "Simultaneous air/fuel-phase PIV measurements in a dense fuel spray," *Experiments in Fluids*, 35, pp. 112-115.

Dykhno, L.A., Williams, L.R. Hanratty, T.J., 1994, "Maps of Mean Gas Velocity for Stratified Flows with and without Atomization," *International Journal of Multiphase Flow*, 20, No. 4, pp. 691-702.

Flores, A.G., Crowe, K.E., Griffith, P., 1995, "Gas-Phase Secondary Flow in Horizontal, Stratified Annular Two-Phase Flow," *International Journal of Multiphase Flow*, 21, No. 2, pp. 207-221.

Fukano, T. Inatomi, T., 2003, "Analysis of Liquid Film Formation in a Horizontal Annular Flow by DNS," *International Journal of Multiphase Flow*, 29, pp. 1413-1430.

Fukano, T. Ousaka, A., 1989, "Prediction of the Circumferential Distribution of Film Thickness in Horizontal and Near Horizontal Gas-Liquid Annular Flow," *International Journal of Multiphase Flow*, 15, pp. 403-419.

Hagiwara,Y., Esmaeilzadeh, E., Tsutsui, H., Suzuki, K., 1989, "Simultaneous measurement of liquid film thickness, wall shear stress and gas flow turbulence of horizontal wavy two-phase flow," *International Journal of Multiphase Flow*, 15, No. 3, pp. 421-431.

Hassan, Y.A., Schmidl, W., Ortiz-Villafuerte, J., 1998, "Investigation of three-dimensional two-phase flow structure in a bubbly pipe flow," *Measurement Science and Technology*, 9, pp. 309-326.

Hetsroni, G., 1982, *Handbook of Multiphase Systems*, Hemisphere Publishing Co., Washington D.C., pp. 2-25 – 2-35.

Hewitt, G.F., Jayanti, S., Hope, C.B., 1990, "Structure of thin liquid films in gas-liquid horizontal flow," *International Journal of Multiphase Flow*, 16, No. 6, pp. 951-957.

Jayanti, S., Hewitt, G.F., White, S.P., 1990, "Time Dependant Behaviour of the Liquid Film in Horizontal Annular Flow," *International Journal of Multiphase Flow*, 16, No. 6, pp. 1097-1116.

Jayanti, S., Wilkes, N.S., Clarke, D.S., Hewitt, G.F., 1990, "The Prediction of Turbulent Flows Over Roughened Surfaces and Its Application to Interpretation of Mechanisms of Horizontal Annular Flow," *Proceedings of the Royal Society of London A*, 431, pp. 71-88.

Kawaji, M., 1998, "Two-phase flow measurements using a photochromic dye activation technique," *Nuclear Engineering and Design* 184, pp. 393-408.

Khalitov, D.A., Longmire, E.K., 2002, "Simultaneous two-phase PIV by two-parameter phase discrimination," *Experiments in Fluids*, 32, pp. 252-268.

Kiger, K.T., Pan, C., 2000, "PIV technique for the simultaneous measurement of dilute two-phase flows," *Journal of Fluids Engineering*, 122, 811-818.

Kraftori, D., Hestroni, G., Banerjee, S., 1995, "Particle behavior in the turbulent boundary layer. II. Velocity and distribution profiles," *Physics of Fluids*, 7, No. 5, pp. 1107-1121.

Lindken, R., Merzkirch, W., 1999, "Velocity measurements of liquid and gaseous phase for a system of bubbles rising in water," within Adrian, R.J., *The third international workshop on PIV*, 1999, Santa Barbara, California, pp. 113-118.

Lindken, R., Merzkirch, W., 2002, "A novel PIV technique for measurements in multiphase flows and its application to two-phase bubbly flows," *Experiments in Fluids*, 33, No. 6, pp. 814-825.

Mei, R., Hu, K.C., "Particle concentration non-uniformity in turbulent flow," within Celata, G.P., Di Marco, P., Shah, R.K., *Two-Phase Modeling and Experimentation 1999*, Vol. 2, pp. 1171-1179, Rome, Italy, May 1999. Edizioni ETS, Piza.

Meinhart, C.D., Wereley, S.T., 2003, "The theory of diffraction-limited resolution in microparticle image velocimetry," *Measurement Science and Technology*, 14, pp. 1047-1053.

Meinhart, C.D., Wereley, S.T., Santiago, J.G., 1999, "PIV measurements of a microchannel flow," *Experiments in Fluids*, 27, pp. 414-419.

Meinhart, C.D., Zhang, H., 2000, "The flow structure inside a microfabricated inkjet printhead," *Journal of Microelectromechanical Systems*, 9, No. 1, pp. 67-75.

Müller, D., Müller, B., Renz, U., 2001, "Three-dimensional particle-streak tracking (PST) velocity measurements of a heat exchanger inlet flow," *Experiments in Fluids*, 30, pp. 645-656.

Müller-Steinhagen, H., Heck, K., 1986, "A simple friction pressure drop correlation for two-phase flow in pipes," *Chemical Engineering Process*, 20, pp. 297-308.

Nowak, M., 2002, "Wall shear stress measurement in a turbulent pipe flow using ultrasound Doppler velocimetry," *Experiments in Fluids*, 33, pp. 249-255.

Khoo, B.C., Chew, Y.T., Teo, C.J., 2001, "Near-wall hot-wire measurements, Part II: Turbulence time scale, convective velocity and spectra in the viscous sublayer," *Experiments in Fluids*, 31, pp. 494-505.

Kundu, P.K., Cohen, I.M., 2004, *Fluid Mechanics*, Elsevier Academic Press, San Diego, California.

LaVision GmbH, 2002, *DaVis Software Seminary: Working with PIV Systems*, June 11 – August 11, 2002.

Olsen, M.G., Adrian, R.J., 2000, "Out-of-focus effects on particle image visibility and correlation in microscopic particle image velocimetry," *Experiments in Fluids*, Supplement, pp. S166-S174.

Ooms, G., Jansen, G.H., 2000, "Particle-turbulence interaction in stationary, homogeneous, isotropic turbulence," *International Journal of Multiphase Flow*, 26, pp. 1831-1850.

Ould Didi, M.B., Kattan, N., Thome, J.R., 2002, "Prediction of two-phase pressure gradients of refrigerants in horizontal tubes," *International Journal of Refrigeration*, 25, pp. 935-947.

Owen, D.G., Hewitt, G.F., 1987, "An improved annular two-phase flow model," *3rd International Conference on Multi-phase Flow*, The Hague, Netherlands, 18-20 May, 1987, pp. 73-84.

Paras, S.V., Karabelas, A.J., 1991, "Properties of the Liquid Layer in Horizontal Annular Flow," *International Journal of Multiphase Flow*, 17, No. 4, pp. 439-454.

Pletcher, R.H., McManus, H.N., 1965, "The Fluid Dynamics of 3-dimensional liquid films with free surface shear: a finite difference approach," *Proceedings of the 9th Midwestern Mechanics Conference*, Madison, WI.

Prasad, A.K., Adrian, R.J., Landreth, C.C., Offutt, P.W., 1992, "Effect of resolution of the speed and accuracy of particle image velocimetry interrogation," *Experiments in Fluids*, 13, pp. 105-116.

Raffel, M., Willert, C., Kompenhans, J., 1998, *Particle image velocimetry*, Springer-Verlag, Berlin-Heidelberg, Germany.

Rodríguez, D.J., Shedd, T.A., 2004, "Entrainment of Gas in the Liquid Film of Horizontal, Annular, Two-Phase Flow," To appear, *International Journal of Multiphase Flow*.

Rottenkolber, G., Gindele, J., Raposo, J., Dullenkopf, K., Hentschel, W., Wittig, S., Spicher, S., Merzkirch, W., 1999, "Spray analysis of a gasoline direct injector by means of simultaneous two-phase PIV," within Adrian, R.J., *The Third International Workshop on PIV*, 1999, Santa Barbara, California, pp. 209-216.

Russ, J.C., 1998, *The Image Processing Handbook*, CRC Press LLC, Boca Raton, Florida.

Russell, T.W.F., Lamb D.E., 1965, "Flow Mechanism of Two-Phase Annular Flow," *The Canadian Journal of Chemical Engineering*, pp. 237-245.

Sakakibara, J., Wicker, R.B., Eaton, J.K., 1996, "Measurements of the particle-fluid velocity correlation and the extra dissipation in a round jet," *International Journal of Multiphase Flow*, 22, pp. 863-881.

Santiago, J.G., Wereley, S.T., Meinhart, C.D., Beebe, D.J., Adrian, R.J., 1998, "A particle image velocimetry system for microfluidics," *Experiments in Fluids*, 25, pp. 316-319.

Shedd, T.A., 1998, "Automated optical liquid film thickness measurement method," *Review of Scientific Instruments*, 69, No. 12, pp. 4205-4213.

Shedd, T.A., 2001, *Characteristics of the liquid film in horizontal two-phase flow*, Doctor of Philosophy Thesis, School of Mechanical Engineering, University of Illinois at Urbana-Champaign.

Shedd, T.A., 2002, "Single and Three-color Strobe Techniques for Bubble/Droplet Sizing and Velocimetry," Proc. 15th ILASS Americas Annual Conference on Liquid Atomization and Spray Systems, May 2002, Madison, WI.

Stevanovic, V., Studovic, M., 1995, "A simple model for vertical annular and horizontal stratified two-phase flows with liquid entrainment and phase transitions: one-dimensional steady state conditions," *Nuclear Engineering and Design*, 154, pp. 357-379.

Sutharson, B., Kawaji, M., Ousaka, A., 1995, "Measurement of Circumferential and Axial Liquid Film Velocities in Horizontal Annular Flow," *International Journal of Multiphase Flow*, 21, No. 2, pp. 193-206.

Tian, J.-D., Hui-He, Q., 2002, "Eliminating background noise effect in micro-resolution particle image velocimetry," *Applied Optics*, 41, No. 32, pp. 6849-6857.

Towers, D.P., Towers, C.E., Buckberry, C.H., Reeves, M., 1999, "A colour PIV system employing fluorescent particles for two-phase flow measurements," *Measurement Science and Technology*, 10, pp. 824-830.

Westerweel, J., 1997, "Fundamentals of digital particle image velocimetry," *Measurement Science and Technology*, 8, pp. 1379-1392.

Whalley, P.B., 1987, *Boiling, Condensation, and Gas-Liquid Flow*, Clarendon Press, Oxford, United Kingdom.

Woodmansee, D.E., Hanratty, T.J., 1969, "Mechanism for the Removal from a Liquid Surface by a Parallel Air Flow," *Chemical Engineering Science*, 24, pp. 299-307.

Yarin, L.P., Hetsroni, G., 1994, "Turbulence intensity of dilute two-phase flows: Part I-III," *International Journal of Multiphase Flow*, 20, pp. 1-44.